J. Fluid Mech. (2001), *vol.* 449, *pp.* 1–37. © 2001 Cambridge University Press
DOI: 10.1017/S0022112001006358 Printed in the United Kingdom

Zonal approach to centrifugal, elliptic and hyperbolic instabilities in Stuart vortices with external rotation

By FABIEN S. GODEFERD[1], CLAUDE CAMBON[1] AND S. LEBLANC[2]

[1]Laboratoire de Mécanique des Fluides et d'Acoustique, UMR 5509, École Centrale de Lyon, BP 163, 69131 Ecully Cedex, France

[2]Département de Mathématiques, Université de Toulon et du Var, BP 132, F-83957 La Garde Cedex, France

(Received 12 April 2000 and in revised form 22 April 2001)

The stability analysis of a street of Stuart vortices in a rotating frame is performed by integrating the Kelvin–Townsend equations along the mean flow trajectories, using the geometrical optics technique (Lifschitz & Hameiri 1991) for short-wave perturbations. A parallel is drawn between the formulations of this zonal approach and that of rapid distortion theory, better known to the turbulence community. The results presented confirm those obtained by the standard stability analysis based on normal-mode decomposition: depending on the rotation parameter and the oblique mode considered, three unstable zones are identified, related to the centrifugal, elliptic and hyperbolic instabilities, as observed for Taylor–Green cells (Sipp *et al.* 1999). Anticyclonic rotation is shown to destabilize Stuart vortices through a combination of the elliptical and centrifugal instability mechanisms, depending on the ratio of its rate to the structure core vorticity. Available stability criteria are discussed in the general case of two-dimensional rotating flows, in relation to their streamline topology and the values of the local Rossby number or vorticity.

1. Introduction

System rotation does not affect the motion of an incompressible two-dimensional flow but it alters its stability with respect to three-dimensional disturbances. Base flows consisting of arrays of vortices are suitable candidates for a more closely focused study. Hence, for a rotating frame, one finds both co-rotating and counter-rotating vortices, otherwise denoted cyclonic and anticyclonic, respectively. From experimental and numerical studies, it is now well known that moderately strong anticyclones are preferentially destabilized (Hopfinger & van Heijst 1993); however we feel that explanations for this phenomenon, and precise ranges of parameters, especially for the Rossby number, are often incomplete in the literature.

Pure parallel flow with system rotation, e.g. the rotating plane channel, is a well known instance of anticyclonic destabilization. The related conventional stability analyses have adressed the case of a hyperbolic tangent profile in a rotating frame. We shall not discuss such analyses since this case is well documented (see Johnson 1963; Pedley 1969; Bradshaw 1969; Yanase *et al.* 1993; Leblanc & Cambon 1997), and marginal with respect to our study, with concentrated vortices.

With the insight provided by the abundant literature existing on the problem of

vortex destabilization, ranging from theoretical analyses to physical and numerical experiments, we revisit the topic in this paper by studying the linear stability of a simple *non-parallel* flow with system rotation, namely a street of Stuart vortices. Indeed, the thorough knowledge of the domain of stability of Stuart vortices without rotation is of interest since it constitutes an interesting model for the sheared mixing layer with spanwise billows (Stuart 1967). Even though the exact streamlines are not the same, the shapes of the Stuart and mixing layer vortices are sufficiently close to justify an extended study of the former. In the rotating case the shear layer instability is different, but knowing how an array of existing Stuart vortices behaves under the effect of external rotation is still of interest, especially from the more general stability criteria obtained in the study.

We now review briefly results of studies that started with a simpler, and more 'academic' context: Sipp, Lauga & Jacquin (1999) have studied a periodic array of two-dimensional Taylor–Green vortices with either square or rectangular aspect ratio, so that the core of the vortices may be exactly circular or squeezed in one direction. In the latter case, three types of short-wave instability may arise, whereas the square case prohibits the appearance of the so-called elliptic instability, for the core of the Taylor–Green vortices remains circular.

The flow constituted by a two-dimensional array of Taylor–Green vortices is periodic in both x_1- and x_2-directions, say. The basic cell is a square, and consists of four rolls bounded by squared streamlines, and counter-rotating with respect to one other: this corresponds to Taylor's 'four-roller mill' (Lagnado & Leal 1990). In addition, ellipticity can be introduced by considering a rectangular cell of aspect ratio E, and the flow can be set in a rotating frame with angular velocity Ω along the axis of the Taylor–Green vortices. When $\Omega \neq 0$, two non-adjacent vortices are cyclonic and the two others are anticyclonic. In non-dimensional form, we recall that the streamfunction is given by $\psi = (\sin x_1 \sin x_2)/(1 + E^2)$ and the Rossby number is $Ro = W_0/(2\Omega)$, with W_0 the absolute value of the core vorticity. This definition of Ro (Cambon *et al.* 1994) will be used throughout the paper. Note that Ro is algebraic with $Ro < 0$ for anticyclonic eddies. (The non-rotating case corresponds to $|Ro| = \infty$.)

A preliminary study of the rotating case using large-eddy simulation (Cambon *et al.* 1994) at $E = 1$ showed the preferential destabilization of anticyclonic vortices at $Ro = -2$, and stabilization both in the cyclonic case and in the case of zero absolute vorticity at the core $Ro = -1$. As in that work, Leblanc & Godeferd (1999) use numerical simulations to illustrate the link between the ribs appearing between the Taylor–Green vortices, and the presence of hyperbolic instability. In the non-rotating case, both linear stability analysis and direct numerical simulations were performed by Lundgren & Mansour (1996) for an *isolated* vortex enclosed within free-slip walls, by using symmetrized Fourier components for the disturbance field. Their method is therefore not suitable to study the dissymetry (cyclonic–anticyclonic) induced by system rotation on the whole four-roller mill, as shown by Sipp *et al.* (1999).

Complete three-dimensional stability analyses in the circular $E = 1$ and elliptic case $E = 2$, were achieved by Sipp & Jacquin (1998) and Sipp *et al.* (1999), including the effect of system rotation. The latter work includes a detailed study of the three background instabilities, with a particular emphasis on the centrifugal one, which is activated only in the presence of anticyclonic system rotation. These studies offer a quantitative comparison of the local analysis or 'geometrical optics' (Lifschitz & Hameiri 1991) for short-wave disturbances localized around mean trajectories, with a more classical non-local analysis in terms of normal modes in the following form for the velocity and pressure disturbances: $\mathrm{e}^{st}\mathrm{e}^{\mathrm{i}k_3x_3} f(x_1, x_2)$, for a mode of spanwise

wavevector component k_3. The main result is the precise identification by *both* methods of a centrifugal mode of instability.

Returning to our application of interest here, the street of Stuart vortices, let us first recall that Pierrehumbert & Widnall (1982) performed spectral linear stability calculations in the non-rotating case, discovering the so-called 'translative' modes, which are outside the scope of the present paper, since they correspond to a long-wavelength interaction between adjacent vortices. In the short-wavelength approximation, Leblanc & Cambon (1998) have used two different approaches for studying the stability of Stuart vortices in a rotating frame. First, the geometrical optics stability theory was applied to obtain analytical stability criteria in relation to stagnation points, thus overlooking what may happen in the surrounding areas, e.g. possible centrifugal instabilities. In their normal-mode computations, the ellipticity was probably too strong, and perhaps the number of numerical modes employed too low, for them to be able to bring to light this type of instability.

Potylitsin & Peltier (1999) have studied the same problem of Stuart vortices in a rotating frame, but using only a normal-mode analysis for studying their stability. With this *global* approach, they seem to have been able to identify the centrifugal instability, though it may be a localized phenomenon. The usefulness of the local method we use here, versus more classical global normal-mode analyses, lies in the fact that it can 'isolate' a given instability mechanism, which is more difficult with numerical eigenvalue calculations.

Recently, Sipp & Jacquin (2000) have applied their generalized criterion for centrifugal instability to the Stuart vortices. Le Dizès (2000) gave an analytical formula for the elliptical instability in a rotating frame, valid at weak ellipticity and large wavenumber, and proposed an interesting correction when the spanwise wavelength k_3 of the instability is moderate. His method yields a matching between different results from Leblanc & Cambon (1998) and Potylitsin & Peltier (1999) at different k_3 values (2, 10, ∞), which we shall discuss later.

We present in the following section a reminder of the physical principles and canonical flows for the three instability types. The role of those specific modes that do not act by means of pressure is discussed in § 2.4. The methodology for zonal analysis is presented in § 3, in which we detail the simplified linearized model (§ 3.1), and the short-wave analysis using WKB theory (§ 3.2). Equations and numerical resolution for the model are presented in §§ 3.3 and 3.4. Then, results are thoroughly described in § 4 for carefully chosen sets of parameters relevant to the rotating Stuart vortices flow. A synthesis of the results for rotating two-dimensional vortices instabilities is proposed in § 5, and concluding remarks given in § 6.

2. Description of the three background instabilities

The observed phenomenon of 'asymmetrization' by solid body rotation of a flow containing both cyclonic and anticyclonic vortices is *a priori* the result of a superposition of the three instability mechanisms described below, at least as far as can be identified by linear theory.†

First, we consider an infinite circular vortex which is fully described by its radial distribution of vorticity $W(r)$, or the circulation $\Gamma(r)$. Previous classical works have

† By asymmetrization, we mean here that the three-dimensional instability mechanisms of cyclones and anticyclones by the background rotation are different. This is not to be confused with the process of non-axisymmetrization of a two-dimensional circular vortex.

brought to light two possible inertial instability mechanisms (Drazin & Reid 1981; Kloosterziel & van Heijst 1991). The first is ruled by Rayleigh's circulation criterion; it is a centrifugal inertial instability that may appear at a maximal point for the *circulation*. The second one is a barotropic instability related to an extremum in the *vorticity* profile, which, in terms of the radial *velocity* profile, translates into an inflectional point. However, the latter mechanism only amplifies two-dimensional perturbations, that are known to remain unaffected by system rotation; it is therefore disqualified from explaining the asymmetry of cyclones and anticyclones containing rotating flows.

The simplest canonical flow for discussing the centrifugal instability is a pure circular flow entirely specified through a radial distribution of the velocity $V(r)$, or of the vorticity $W(r)$, or of the circulation distribution $\Gamma(r)$.

For elliptic and hyperbolic instabilities, the corresponding canonical flow is called *extensional* (see § 3), i.e. a plane flow which is unbounded and possesses space-uniform mean velocity gradients with symmetric and skew-symmetric components respectively characterized by S and Ω_0 (see equation (3.5)), the latter amounting to half the vorticity W_0.

Considering an array of Taylor–Green vortices or a street of Stuart vortices, two main topological features need to be accounted for in the stability properties of these flows: the possible ellipticity of the stagnation point located on the axis of the vortices, and the hyperbolic one in between them. Both are associated with given modes of instability, as follows. In the coming sections, the three instabilities are presented, from the simplest centrifugal instability to the more complex elliptic and hyperbolic ones.

2.1. *Centrifugal instability in the rotating frame*

Starting from the classic criterion for a circular vortex of azimuthal velocity $U(r)$ and vorticity $W(r)$, expressed in a Galilean frame of reference, Kloosterziel & vanHeijst (1991) have drawn an extended one that is valid in a frame rotating at rate Ω. We define the absolute circulation as

$$\Gamma_a(r) = 2\pi r^2 \left(\Omega + \frac{U(r)}{r} \right), \tag{2.1}$$

and the generalized discriminant as

$$\Phi(r) = \frac{1}{4\pi^2 r^3} \frac{\mathrm{d}\Gamma_a^2}{\mathrm{d}r} = 2 \left(\Omega + \frac{U(r)}{r} \right) (W + 2\Omega), \tag{2.2}$$

meaning that the instability is located around circular trajectories where Φ becomes negative after changing sign.

When $U(r)$ characterizes a standard distribution, whose circulation $\Gamma(r) = 2\pi r U(r)$ varies monotonically from 0 at the centre – such that $\Gamma(r) \sim 2\pi r^2 \Omega_0$ in its neighbourhood – to a finite value Γ_∞ as $r \to \infty$, clearly no instability can occur in the fixed frame case. This situation is unchanged in a rotating frame with cyclonic system rotation, since a monotonic system circulation is added to the monotonic relative circulation. In contrast, when the basic rotation is anticyclonic with $\Omega < \Omega_0$, the absolute circulation becomes positive near the centre and negative far away, assuming $\Omega_0 > 0$ without loss of generality. This combination of parameters can therefore lead to the triggering of a centrifugal instability. One then gets the quite simple picture that vortices with simple radial distribution of relative circulation are destabilized by a centrifugal instability through anticyclonic basic rotation, provided that the local Rossby number at the

core be $Ro < -1$. In this inequality, we have chosen to use the Rossby number based on the core vorticity of the eddies, yielding $Ro = W_0/(2\Omega)$, which also amounts to comparing the rotation rate of the vortices to the external rotation: $Ro = \Omega_0/\Omega$.

2.2. *Elliptic instability in the rotating frame*

The elliptic instability has its origin in the presence of elliptic stagnation points, i.e. somewhat differently from the previous centrifugal instability phenomenon that requires extending the analysis to a wider domain in the vortex.

Elliptic instability is often characterized as a cooperative instability which results from the weak additional strain induced by two adjacent vortices, according to works since 1975 (see Moore & Saffman 1975, Tsai & Widnall 1976, Pierrehumbert & Widnall 1982 and Leweke & Williamson 1998 for a historical survey and recent works). More generally, one may simply assume a single vortex with elliptic streamlines (Pierrehumbert 1986). Considering a base flow with uniform mean velocity gradients $U_{i,j}$, the simplest method for studying its stability is to solve the Kelvin–Townsend equations for three-dimensional disturbances in terms of Lagrangian Fourier modes, as done in rapid distortion theory (RDT), with recent application to classic stability analysis (see Cambon & Scott 1999 for a review). The constant velocity gradient matrix $U_{i,j}$ in the two-dimensional case is here decomposed into a strain rate S and an angular velocity Ω_0 of half the vorticity, chosen positive without loss of generality: $S < \Omega_0$ in the elliptic case; $S > \Omega_0$ in the hyperbolic case. At weak ellipticity $S \ll \Omega_0$, the disturbances can be described as unbounded plane inertial waves with the dispersion relation $\omega = \pm 2\Omega_0 \cos\theta$. The angle θ is measured between the wave vector and the axis perpendicular to the plane of the mean flow. Resonance is found for $\omega = \Omega_0$, resulting in the selective amplification of oblique modes at $\cos\theta = \pm 1/2$ by a Floquet mechanism (Bayly 1986; Waleffe 1990). In the rotating frame, the angle of the most unstable oblique modes and the Floquet coefficient that expresses their exponential amplification are obtained from

$$\cos\theta = \pm\frac{1}{2}\frac{Ro}{(1+Ro)} \tag{2.3}$$

and

$$\frac{\sigma}{S} = \frac{1}{16}\left(\frac{3Ro+2}{Ro+1}\right)^2. \tag{2.4}$$

The first equation is obtained by replacing the vorticity $2\Omega_0$ by the absolute vorticity $2\Omega + 2\Omega_0$ in the resonance condition (Craik 1989), whereas the second is a recent generalization by Le Dizès of the 9/16 value found by Waleffe in the non-rotating case (or $Ro = \pm\infty$) (Le Dizès 2000).† At significant ellipticity, the role of basic rotation, which shifts the range of oblique modes and modifies the amplification rate, is not significantly different from the one for $E \sim 1$, as illustrated by Cambon *et al.* (1994). Unfortunately, analytical quantitative relations such as (2.3) and (2.4) cannot be obtained easily except for the close-to-circular $E \sim 1$ case.

From equation (2.3) one finds that no θ angle can be computed in the range $-2 < Ro < -2/3$, corresponding to a band in which no elliptic instability may appear. Equation (2.4) then provides the evolution of the amplification with the rotation parameter (see the diagram of figure 1): strong anticyclones are destabilized

† As explained in detail by Le Dizès (2000), these formulae provide parameters – angle and amplification – of the most unstable modes at fixed Ro, though there exists an interval of unstable angle. Conversely, given fixed θ, there is an interval of unstable Rossby number around the peak.

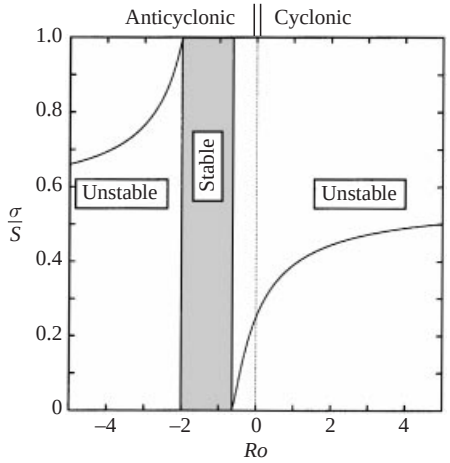

FIGURE 1. Schematic of the stability diagram obtained from equations (2.3) and (2.4). The curves show the evolution of σ/S with respect to the value of the Rossby number. The shaded region indicates the zone over which no elliptic unstable mode is found.

up to $Ro = -2$ where the growth of the perturbation is maximal. With increasing Rossby number, destabilization reappears at values larger than $-2/3$, and cyclonic vortices are destabilized again with infinitely increasing growth when $Ro \to \infty$.

Upon examination of the stability diagram plotted on figure 1, one sees that equation (2.4) has a trifling unexpected behaviour of σ/S for vanishing Rossby number (rapid rotation): the curve is expected to go to zero at $Ro = 0$; however the ratio σ/S vanishes only at $Ro = -1$. Indeed, we see from (2.3) that when $Ro = 0$, the initial orientation of the wave vectors corresponding to parametric instability is $\theta = \pm\pi/2$ corresponding to two-dimensional perturbations, which are *not* affected by the background rotation, and are *stable* (see for instance Leblanc & Cambon 1998). Furthermore, the bandwidth of instability becomes infinitely narrow when $|Ro| \to 0$ (see Bayly, Holm & Lifschitz 1996; Le Dizès 2000). This apparent paradox may be avoided by using the rotation rate as the characteristic time scale in the evolution equation for the kinetic energy of the perturbation (see details in Lebovitz & Lifschitz 1996), so that it may be rigorously shown that the case of infinite rotation ($Ro = 0$) is stable.

2.3. *Hyperbolic instability in the rotating frame*

The hyperbolic stretching mechanism was illustrated by the seminal work of Batchelor & Proudman (1954) in homogeneous RDT, in studying vorticity disturbances to a base flow with constant velocity gradient $U_{i,j}$. In the particular two-dimensional irrotational case, where $\Omega_0 = 0$, vorticity disturbances are governed by a Cauchy equation, which exhibits exponential amplification of vorticity along the axis of stretching. Similar exponential growth also appears when looking at the Fourier modes of the velocity disturbance, especially for pure spanwise modes. This result is not significantly changed in the general hyperbolic case $S > \Omega_0 \neq 0$, a two-dimensional rotational flow (Cambon 1982, Lagnado, Phan-Thien & Leal 1984). When adding background rotation at rate Ω, this exponential amplification can be cancelled for a sufficiently high value of Ω, as discussed in the following. However, insofar as asymmetry is created in flows with cyclonic and anticyclonic vortices, hyperbolic stretching does not appear to be a good explanatory phenomenon. Regarding the impact of such

exponential amplification on more complicated base flows, nonlinear studies suggest that hyperbolic stretching only concentrates the energy of the disturbance though without affecting the energy of the background. This discussion, whether hyperbolic stretching is associated with a genuine instability in actual flows, is outside the scope of the present paper, but leads to considering with caution results of linear stability when hyperbolic zones are involved (Kerr & Dold 1994; Waleffe, private communication).

2.4. *The role of pure transverse, pressureless modes*

The role of pressureless modes of instability was emphasized by Bayly (1988) for centrifugal instability and by Leblanc & Cambon (1997) in connection with generalized criteria. These works helped to clear up how the same criterion can be derived from a rigorous stability analysis (Pedley 1969) and from a semi-empirical, apparently two-dimensional and pressureless analysis (Bradshaw 1969; Bidokhti & Tritton 1992). Spanwise modes may be written as

$$u_i(x_1, x_2, x_3, t) = \tilde{u}_i(x_1, x_2, t)\mathrm{e}^{\mathrm{i}k_3 x_3} \tag{2.5}$$

where the length scale $1/k_3$ is much larger than the two other ones in the (x_1,x_2)-plane of the mean flow. Such modes satisfy the incompressibility constraint without being affected by the pressure disturbance. In the strict two-dimensional limit, i.e. $k_3 = 0$, things are radically different: while spanwise modes have space variability concentrated in the spanwise direction, two-dimensional modes have variability concentrated in the two other directions. Simplified pressureless dynamics is physically incorrect for the complete velocity field u_i, e.g. the use of a 'displaced particle' analysis (Tritton 1988). But replacing u_i by $\tilde{u}_i$ is allowed and permits correct dynamics to be retrieved, leading to identical simplified equations and thus to the same criterion. For two-dimensional extensional flows in a rotating frame, the dynamics of transverse, pressureless modes yields the following generalization of the Bradshaw–Richardson discriminant for parallel flows, $\Phi = 2\Omega(2\Omega - \mathrm{d}U_1/\mathrm{d}x_2)$:

$$\Phi = -S^2 + (\Omega_0 + 2\Omega)^2 \tag{2.6}$$

with $\exp(\sqrt{-\Phi}t)$ amplification; it suggests maximum destabilization for a typical Rossby number $Ro = -2$. Notice here the *tilting* vorticity $\Omega_0 + 2\Omega$ discussed in Cambon *et al.* (1994), which differs from the *absolute* vorticity $2\Omega_0 + 2\Omega$.

3. Methodology for zonal stability analysis

3.1. *The linearized model equations*

Let us recall the basic equations for an incompressible inviscid flow, assuming the usual mean/fluctuating decomposition for the velocity and the pressure. The Euler equation for the mean velocity $\boldsymbol{U}$ and pressure P is

$$\frac{\partial U_i}{\partial t} + U_j \frac{\partial U_i}{\partial x_j} = -\frac{\partial P}{\partial x_i}. \tag{3.1}$$

For the fluctuating velocity field $\boldsymbol{u}$ and pressure p, the linearized equation becomes

$$\frac{\partial u_i}{\partial t} + U_j \frac{\partial u_i}{\partial x_j} + u_j \frac{\partial U_i}{\partial x_j} = -\frac{\partial p}{\partial x_i} \tag{3.2}$$

and $\nabla \cdot \boldsymbol{u} = 0$.

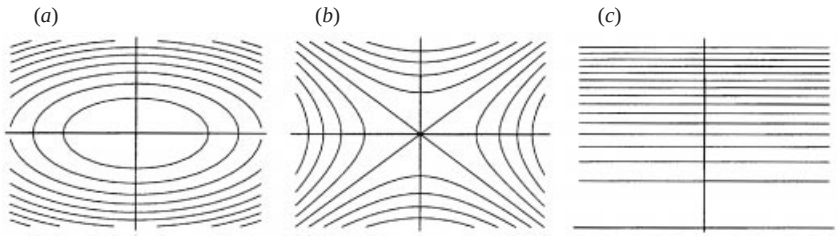

FIGURE 2. Schematics of the streamlines in flows dominated by (*a*) vorticity (elliptical streamlines, here with $\Omega_0/S = 2$), (*b*) strain (hyperbolic, $\Omega_0/S = 0$) and (*c*) shear (parallel streamlines, $\Omega_0/S = 1$).

As a common background, homogeneous† RDT (see Townsend 1976) and recent linear stability analyses (for instance Lagnado *et al.* 1984; Craik & Criminale 1986) deal with the time-development of a disturbance field (u_i, p) evolving in the presence of an oversimplified base flow (U_i, P), with

$$U_i = \lambda_{ij}(t)x_j. \tag{3.3}$$

This flow with space-uniform velocity gradient will be referred to as an *extensional* flow. For a base flow of this form to be a particular solution of Euler equations (3.1) requires (Craya 1958) that the matrix of ij-components

$$\frac{\mathrm{d}\lambda_{ij}}{\mathrm{d}t} + \lambda_{ik}\lambda_{kj} \tag{3.4}$$

be symmetric and that $\lambda_{ii} = 0$. Rotational mean flows yield more complicated linear solutions for disturbances than irrotational ones, and only the steady case has received much attention (see Bayly *et al.* 1996, and Leblanc 2000 for recent developments in unsteady cases). The above conditions (3.3)–(3.4) imply that λ_{ij} is written as

$$\boldsymbol{\lambda} = \begin{pmatrix} 0 & S - \Omega_0 & 0 \\ S + \Omega_0 & 0 & 0 \\ 0 & 0 & 0 \end{pmatrix} \tag{3.5}$$

in the steady, rotational case, when axes are chosen appropriately, where $S, \Omega_0 \geqslant 0$. This corresponds to steady plane flows, combining vorticity $2\Omega_0$ and irrotational straining S. The related streamfunction is

$$\psi = -\frac{S}{2}(x_1^2 - x_2^2) + \frac{\Omega_0}{2}(x_1^2 + x_2^2). \tag{3.6}$$

Depending on the relative values of S and Ω_0, streamlines in the base flow may be of elliptical or hyperbolic shape, and in the case of vorticity entirely compensated by strain, be straight lines in a parallel flow, as schematically pictured on figure 2.

The disturbance fields (u_i, p) satisfy the modified Euler equation (3.2) with the advection–distortion parts written in terms of λ_{ij}. Its linear solution is most easily obtained via Fourier analysis. An elementary Fourier component of the form ($\mathrm{i}^2 = -1$)

$$u_i = a_i(t)\exp[\mathrm{i}\boldsymbol{k}(t)\cdot\boldsymbol{x}] \tag{3.7}$$

yields a solution of the problem if $\boldsymbol{k}$ and a_i satisfy a linear system of simple ordinary differential equations, referred to as Townsend equations. The pressure fluctuation, which is a solution of a Poisson equation, is given by an algebraic relationship in terms of a_i. Decomposing turbulence into Fourier components, usually referred to as

† In the non-homogeneous case, a Reynolds stress tensor term would appear in equation (3.1).

spectral analysis, allows a straightforward treatment of the non-local dependence of pressure upon velocity, which leads to the appearance of spatial integrals if spectral analysis is not used. In this way, the problem of non-locality is rendered relatively innocuous.

Time dependence of the wavenumber represents the convection of the plane wave $\exp[\mathrm{i}\boldsymbol{k}(t)\cdot\boldsymbol{x}]$ by the base flow. Both the direction and magnitude of $\boldsymbol{k}$ change as wavecrests rotate and approach, or separate from, each other due to mean velocity gradients. If $\boldsymbol{k}$ is given at some time t, it can be related to its value at any other time t_0, $\boldsymbol{K}\equiv\boldsymbol{k}(t_0)$, by

$$K_i = F_{ji}(t,t_0)k_j, \tag{3.8}$$

where the matrix $\boldsymbol{F}$ characterizes the deformation of an imaginary material convected at the mean velocity (3.3), between times t_0 and t. In the language of continuum mechanics, this is the Cauchy tensor associated with deformation by the base flow. Likewise, the solution of the Townsend equations with the above time evolution for $\boldsymbol{k}$ in (3.8) has the form

$$a_i[\boldsymbol{k}(t),t] = G_{ij}(\boldsymbol{k},t,t_0)a_j[\boldsymbol{k}(t_0),t_0], \tag{3.9}$$

where G_{ij} is a spectral Green's function, which is a real *deterministic* quantity.

At this stage, it may be noticed that homogeneous RDT includes enough features to solve the following two problems:

A *deterministic problem*, which consists in solving the initial value linear system of equations for a_i, in the more general way. This is done by determining the spectral Green function, which is also the key quantity requested in linear stability analysis.

A *statistical problem* which is useful for the prognostic of statistical moments of u_i and p. Interpreting the initial amplitude $a_j(\boldsymbol{K},t_0)$ as a random variable with a given dense $\boldsymbol{K}$-spectrum, equation (3.9) yields the prediction of statistical moments by products of the basic Green's function.

Possible applications to statistics are outside the scope of this paper. Note that solutions (3.9) are valid even if the nonlinear term is not discarded *a priori*, provided that the perturbation consists of a single mode, since a single Fourier mode cannot interact with itself (Craik & Criminale 1986). Exactly the same deterministic problem as the one of homogeneous RDT was addressed in the context of flow stability, although the two communities seem to be largely unaware of each other's work. For instance, the stability analysis in terms of time-dependent, distorted, Fourier modes is attributed to Kelvin (1887) by the stability literature. Owing to the generality of the RDT formulation, which is not restricted to the special case of parallel pure shear flows (as in Kelvin's work), we propose to refer to (3.7)–(3.8) as 'Lagrangian Fourier modes', governed by 'Townsend's equations' (Cambon 2000).

Upon examination of definitions (3.5) and (3.6), three types of flow problems can be isolated. First, the special case $S = 0$ yields pure rotation, which is perhaps better treated in the rotating frame of reference and leads to inertial waves and hence oscillating solutions. Second, the general RDT problem with arbitrary S and Ω_0 was analysed by Cambon (1982). Finally, the limiting case $S = \Omega_0$ (Townsend 1976) corresponds to simple shearing, as shown by (3.6). It is the border between two distinct regimes: one with $S < \Omega_0$, for which the mean flow streamlines are closed and elliptic about the stagnation point at the origin; and the case of $S > \Omega_0$, with open and hyperbolic streamlines (see figure 2).

For $S < \Omega_0$, an illustration of the closeness between RDT and stability analyses is shown on figure 3, to be compared with the location θ_{peak} of elliptic instabilities

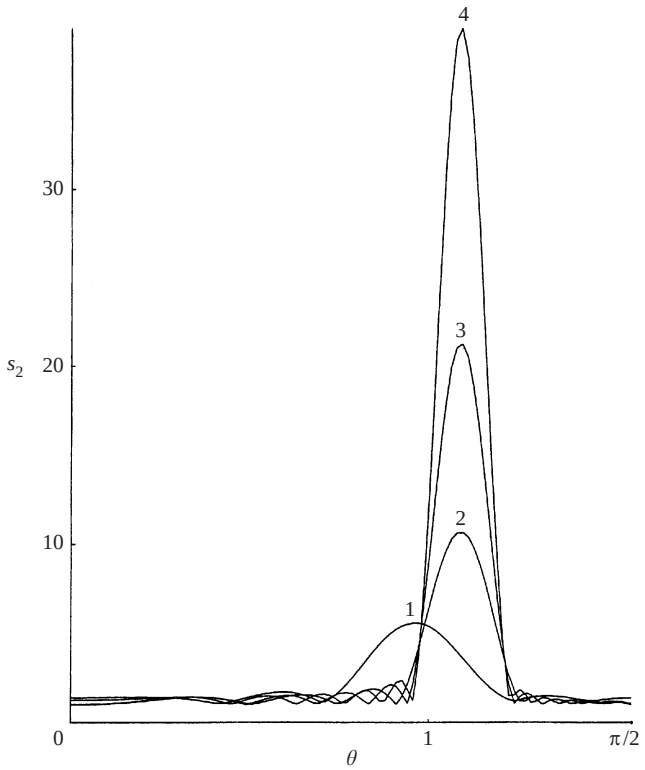

FIGURE 3. For a flow with elliptical streamlines, maximum eigenvalue s_2 of the symmetrized matrix of the Green's function $\mathbf{G}\mathbf{G}^T$ as a function of the direction θ of the wavevector measured from the polar axis. (Taken at a period $t = T$, s_2 differs only from the actual Floquet parameter because of the use of a symmetrized matrix.) Curves labelled 1, 2, 3, 4 are obtained at cumulated deformation of $St = 2.89, 4.22, 5.55, 6.66$ respectively, or in terms of the period $T = 2\pi/\sqrt{\Omega_0^2 - S^2}$: $t/T = 1.3$, 2, 2.5, 3. The ratio of angular velocity to deformation Ω_0/S is 3 (from Cambon 1982). The location of the peak corresponds to the predicted $\theta = \pi/3$, as mentioned in § 1.

shown later on in the text. Figure 3 was obtained by Cambon (1982) and shows that Townsend's equations in the case of exactly elliptical streamlines can generate angular peaks of instability.

3.2. *Principles of the zonal approach through scale separation*

Even if the Green's function related to the canonical base flow can give interesting information for linear stability analysis and short-time development of turbulence, this problem is somewhat unphysical in the absence of typical length scales for variation of the base flow gradients and disturbances length scales. For instance, the Green's function in (3.9) only depends on the orientation, not on the modulus k of the wave vector, and this type of instability, recovered in the weakly elliptical case $S \ll \Omega_0$, was called 'broadband' by Pierrehumbert (1986). The Widnall instability (Tsai & Widnall 1976), which is an actual occurrence of the generic elliptical instability, appears at short wavenumbers. Rather than considering perturbations with arbitrary wavelength k^{-1} in the presence of the extensional flow, it is more physical to consider a base flow whose velocity gradients vary over a typical length scale L, and to restrict the validity of the zonal stability analysis to perturbations of much shorter wavelength $k^{-1} \ll L$. In so doing, the disturbance field should locally experience advection and distortion

effects by the base flow, similarly to the effects of an extensional flow. Given *a priori* a length scale separation between base and disturbance flows, one can imagine looking through a mathematical magnifying glass at the vicinity of real base trajectories. This idea was formalized by Lifschitz & Hameiri (1991) using an asymptotic approach based on the classical WKB method, which is traditionally used to analyse the ray theoretic limit in wave problems, i.e. at short waves (see e.g. Lighthill 1978). The perturbation field solution is formally written as

$$u_i(\boldsymbol{x},t) = a_i(\boldsymbol{x},t)\exp[\mathrm{i}\phi(\boldsymbol{x},t)/\epsilon] \tag{3.10}$$

with a similar expression for the fluctuating pressure; ϕ is a real phase function and ϵ is a small parameter expressing the smallness of scale of the waves represented by (3.10). Their complex amplitude $a_i(\boldsymbol{x},t)$ is expanded in powers of ϵ according to the WKB technique. Over distances of $O(\epsilon)$, one can use a spatial Taylor series representation for ϕ – here restricted to the linear term – and approximate a_i as constant. It is then apparent that (3.10) is locally a plane-wave Fourier component of wavenumber

$$k_i(\boldsymbol{x},t) = \epsilon^{-1}\frac{\partial\phi}{\partial x_i}. \tag{3.11}$$

The amplitude $a_i(\boldsymbol{x},t)$ in (3.10) and the corresponding equation for the fluctuating pressure are expanded as a series in powers of ϵ, and the result inserted into the linearized equations without viscosity. At leading order, one finds that

$$\dot{\phi} = \frac{\partial\phi}{\partial t} + U_j\frac{\partial\phi}{\partial x_j} = 0, \tag{3.12}$$

i.e. the wave crests of (3.10) are convected by the mean flow. The spatial derivative of (3.12) yields

$$\dot{k}_i = -\lambda_{ji}(t)k_j \tag{3.13}$$

where, as before, $\lambda_{ij} = \partial U_i/\partial x_j$ and the dot represents the mean-flow material derivative $\partial/\partial t + U_i\partial/\partial x_i$. To next order, one obtains

$$\dot{a}_i^{(0)} = -(\delta_{in} - 2k_ik_n/k^2)\lambda_{nj}(t)a_j^{(0)} \tag{3.14}$$

after elimination of the pressure using the leading-order incompressibility condition $k_ia_i^{(0)} = 0$, where $a_i^{(0)}$ is the leading-order term in the expansion of a_i.

Equations (3.13) and (3.14) have exactly the same form as Townsend equations for $\boldsymbol{k}$ and $\boldsymbol{a}$ in (3.7), which therefore describe the weakly inhomogeneous case at leading order. The only difference lies in that, rather than being plain time derivatives, the dots represent base-flow material derivatives. It implies that, in the zonal approach, one should follow convection by the mean flow. In homogeneous RDT, the different classes of disturbances are only labelled by the direction of the initial wave vector $\boldsymbol{K}$, and all trajectories such as ψ = constant in (3.6) are equivalent. In the zonal approach, it is necessary to add the Lagrangian coordinates vector $\boldsymbol{X}$ for labelling different trajectories. In agreement with classic continuum mechanics, one has

$$\mathrm{d}x_i = F_{ij}\mathrm{d}X_j + U_i\mathrm{d}t, \tag{3.15}$$

when differentiating the trajectory equation, so that (3.12) and (3.13) correspond to

$$k_i\delta x_i = K_i\delta X_i, \quad k_i(\boldsymbol{X},t) = F_{ji}^{-1}(\boldsymbol{X},t,t_0)K_j, \tag{3.16}$$

which is a generalization of (3.8). Equation (3.8) itself actually corresponds to $\boldsymbol{k}\cdot\boldsymbol{x} = \boldsymbol{K}\cdot\boldsymbol{X}$. Even if WKB methods are common in stability analysis, their application to fully

three-dimensional disturbances, with both time- and space-dependent wavevectors, is not common, and the canonical homogeneous RDT provides a useful framework to understand the background of geometrical optics.

3.3. *Numerical solution of the zonal approach model*

The trajectories of the Stuart base flow in the (x_1, x_2)-plane are given by the following streamfunction:

$$\psi = \log(\cosh(x_2) - \rho\cos(x_1)) \tag{3.17}$$

where ρ in the range $]0, 1]$ characterizes the vorticity distribution.

The Kelvin–Townsend equations in the rotating frame are

$$\left.\begin{aligned} \dot{x}_i &= U_i \\ \dot{k}_i &= -U_{j,i}k_j \\ \dot{a}_i &= -\left[\left(\delta_{in} - 2\frac{k_i k_n}{k^2}\right) U_{n,j} + 2\left(\delta_{in} - \frac{k_i k_n}{k^2}\right)\epsilon_{nmj}\Omega_m\right] a_j, \end{aligned}\right\} \tag{3.18}$$

respectively the trajectory equation, the eikonal equation, and the amplitude equation. The overdot denotes a Lagrangian (or substantial) derivative following trajectories. In the above system of ODEs, the velocity components U_i and the velocity gradient matrix $U_{i,j}$ are analytically expressed at any point using equation (3.17). This system is solved with given initial data, which we denote by capital letters: the Lagrangian coordinate $\boldsymbol{X}$ is the initial position on the trajectory, $\boldsymbol{K}$ is the related wavevector, and $\boldsymbol{A}$ the related amplitude.

Provided $\boldsymbol{k}(t)$ be periodic (see the subsequent discussion in § 3.4), the general solution for the linear initial-value problem may be expressed after a period T as

$$a_i(\boldsymbol{X}, \boldsymbol{K}, T) = G_{ij}(\boldsymbol{X}, \boldsymbol{K}, 0, T)A_j. \tag{3.19}$$

The Floquet parameter $\sigma(\boldsymbol{X}, \boldsymbol{K})$ is related to the maximum eigenvalue of the Floquet matrix $\mathbf{G}$ through

$$\sigma(\boldsymbol{X}, \boldsymbol{K}) = \log(||\text{max eigenvalue of } \mathbf{G}(\boldsymbol{X}, \boldsymbol{K}, 0, T)||)/T.$$

Both parameter and matrix are therefore identified independently for each trajectory and each initial wavevector. In order to obtain quantitative results, the system of equations is integrated using a fourth-order Runge–Kutta scheme.

3.4. *Parameters and presented quantities*

The base flow is characterized by the value of ρ in equation (3.17). Therefore, the Rossby number is defined as the ratio $Ro = W_0/(2\Omega)$ of the core vorticity to system vorticity, based on

$$W_0 = -(1 + \rho)/(1 - \rho). \tag{3.20}$$

Each closed streamline is labelled by the abscissa x_0 such that $\boldsymbol{X} = (x_0, 0, 0)$ and $0 < x_0 < \pi$. An open trajectory can be labelled by the ordinate y_0, again with $\boldsymbol{X} = (\pi, y_0, 0)$ and $y_0 > 0$. As found by Sipp & Jacquin 1998, choosing the initial wavevector in a plane normal to the initial velocity vector is enough for a complete analysis. Accordingly, $\boldsymbol{K} = (\sin\theta, 0, \cos\theta)$ for a closed trajectory and $\boldsymbol{K} = (0, \sin\theta, \cos\theta)$ for an open one. This choice corresponds in both cases to $\boldsymbol{K} \cdot \boldsymbol{U} = 0$ at the initial time, so that $\boldsymbol{k} \cdot \boldsymbol{U} = 0$ at subsequent times (see Sipp & Jacquin 1998). In that case, the solution of the eikonal equation is bounded and periodic in time. On the other hand, if $\boldsymbol{K} \cdot \boldsymbol{U} \neq 0$ initially, then it may be shown analytically that outside

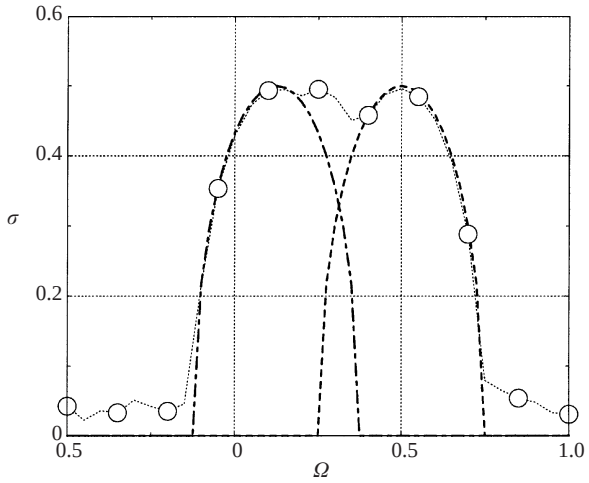

FIGURE 4. Growth rate of the most unstable mode for a Stuart vortex street with rotation as a function of the rotation rate Ω. Dashed curves: asymptotic results for the hyperbolic (left-hand peak) and elliptic (right-hand peak) stagnation points; dotted curves: results from a full linear stability calculation. Parameter for the Stuart vortices: $\rho = 1/3$ (from Leblanc & Cambon 1998).

the hyperbolic stagnation points, the corresponding solution $|\boldsymbol{k}(t)|$ can eventually grow algebraically (see Appendix B). This case is not of interest here, because the periodicity of $\boldsymbol{K}$ is required for equation (3.19) to be an actual Floquet-type problem. As a consequence, the unique parameter for the definition of $\boldsymbol{K}$ is its angle $\theta \in [0, \pi/2]$; the orientation $\theta = 0$ characterizes *pure spanwise* or *pressureless* modes, whereas $\theta = \pi/2$ characterizes two-dimensional modes.

In addition to the Floquet coefficient, $\sigma(x_0, \theta)$ for closed trajectories, $\sigma(y_0, \theta)$ for open trajectories, important quantities are

the local spanwise vorticity $W(x_0)$, or $W(y_0)$, conserved along trajectories,

the relative circulation $\Gamma(x_0)$ of $\boldsymbol{U}$ for closed trajectories in the rotating frame,

the absolute circulation $\Gamma_a(x_0)$,

the local strain rate $S = (\frac{1}{2}[\frac{1}{2}(U_{i,j} + U_{j,i})\frac{1}{2}(U_{i,j} + U_{j,i})])^{1/2}$.

For numerical convenience, the relative and absolute circulation are computed in the same way as system (3.18), by adding to it the equations

$$\dot{\Gamma} = -U^2, \tag{3.21}$$

$$\dot{\Gamma}_a = -U^2 + \Omega(x_1 U_2 - x_2 U_1) \tag{3.22}$$

to be solved along closed trajectories. (The negative sign in front of U^2 comes from the clockwise rotation of the Stuart vortices, opposite to the positive orientation of the (x, y)-plane.) The strain rate varies along trajectories and thus only its order of magnitude is informative. Recall, however, that $S(x_0)$ has a fixed value $S = 1/2$ at the stagnation points, both elliptic and hyperbolic, independent of the vorticity concentration parameter ρ.

Figure 4 shows the results obtained by Leblanc & Cambon (1997) (their figure 7*d*), for the instability growth rates σ versus the external reference frame rotation Ω. It collects results for pure *spanwise* wavevectors, and the two folds in the curve correspond to the growth rates of the elliptic and the hyperbolic instability modes. As seen on this same figure, Leblanc & Cambon (1997) also obtain good agreement of these

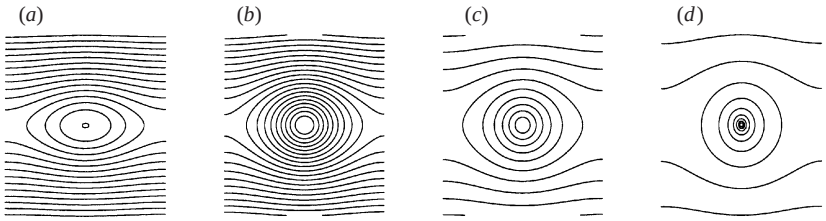

FIGURE 5. Streamlines in the Stuart vortices with parameter $\rho = 1/3,\ 3/4,\ 19/21$ and 1 respectively (a)–(d). (The x and y plotting range is $[-\pi, \pi]$.)

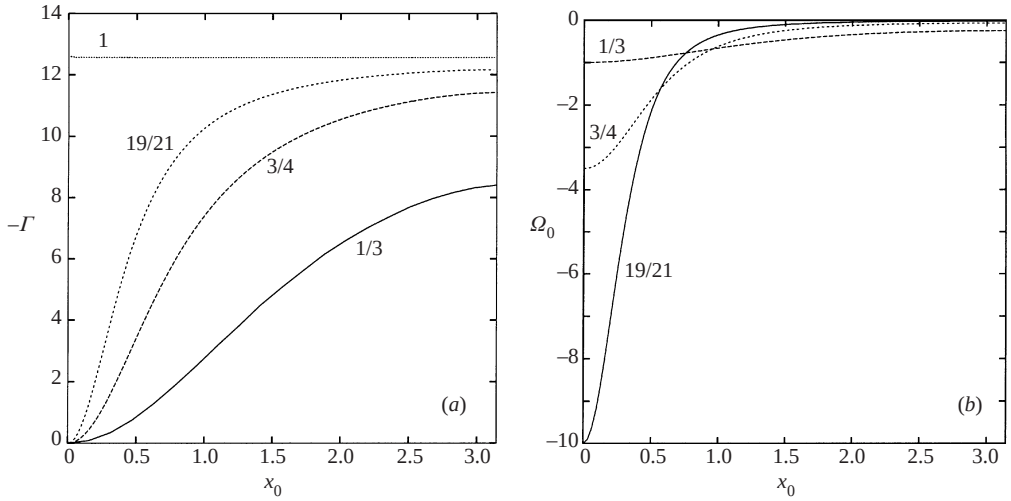

FIGURE 6. (a) Opposite of the relative circulation $-\Gamma$: for decreasing $\rho = 1,\ 19/21,\ 3/4,\ 1/3$. (b) Local spanwise vorticity W for the closed trajectories for decreasing $\rho = 19/21,\ 3/4,\ 1/3$. (In the case $\rho = 1$, the vorticity is infinite at the center, and vanishes everywhere else.)

predictions with results from the normal-mode analysis, using modes expressed as

$$u_i(\boldsymbol{x}, t) = \mathrm{e}^{st}\mathrm{e}^{\mathrm{i}k_3 x_3}\tilde{u}_i(x_1, x_2). \tag{3.23}$$

4. Results

We focus on four different 'geometries' for the Stuart vortices, i.e. using four values for the shape parameter ρ. The streamlines of the Stuart vortices for each of the corresponding four values of ρ are presented on figure 5. The most elliptical, i.e. flattened vortices, is computed with $\rho = 1/3$. For $\rho = 1$, we obtain the 'cylindrical' case, meaning circular core streamlines, while the vorticity concentrates at the unique point $x = 0$. But in this case of course the hyperbolic stagnation point is still present. Two intermediate cases are also taken to be $\rho = 3/4$ and $\rho = 19/21$. Note that these particular values are chosen in order that the corresponding core vorticity W_0 be an integer.

The numerically computed relative circulation Γ, independent of the rotation rate of course, is plotted on figure 6(a). On this figure, we observe that the analytical -4π value is recovered in the $\rho = 1$ singular case, for which the vorticity of the Stuart vortex is a centred Dirac function. For the other three cases, the vorticity is plotted on figure 6(b), again with respect to the x_0-coordinate. When external

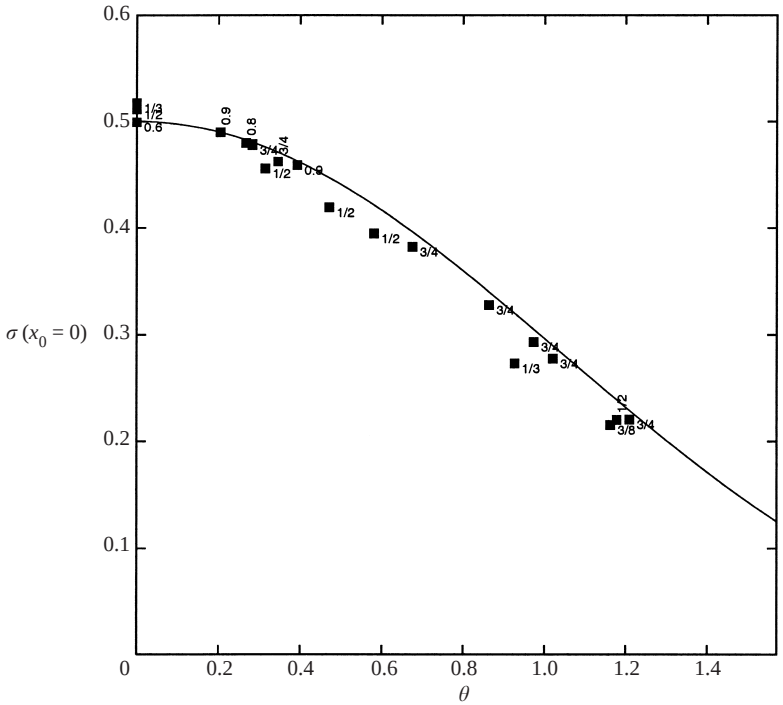

FIGURE 7. Distribution of the Floquet amplification parameter σ for the elliptic instability at the centre of the Stuart vortices, as a function of the angle of maximum destabilization θ given in equation (4.1), plotted with a solid line. Each symbol corresponds to a numerical result obtained with the zonal analysis, for the given value of ρ.

rotation is applied to the system, the absolute circulation is obtained from the relative circulation by adding a parabola to the monotonically increasing curves shown on figure 6(*a*). It is clear that in the anticyclonic case, this contribution ($2\pi\Omega r^2$ in the circular case) is monotonically decreasing, and therefore the two contributions add up to an absolute circulation exhibiting a local extremum. The latter is plotted in the following three-dimensional representation of the Floquet amplification coefficient, in order to emphasize its strong correlation with the region of emergence of a centrifugal instability.

4.1. *Core region*

Looking only at the centre $x_0 = 0$ of the Stuart vortices where $S = 1/2$, equations (2.3) and (2.4) become

$$\sigma(x_0 = 0) = \left(\frac{1 + \cos\theta}{2}\right)^2 S. \tag{4.1}$$

Figure 7 shows this analytical result obtained from a weak ellipticity approximation with numerical results from the zonal analysis close to the elliptic stagnation point $x_0 = 0$. We observe that the agreement is quite good, especially for values of ρ close to 1. However, even for the smaller value $\rho = 1/3$, the departure of the amplification rate from the weakly elliptic prediction is not very great.

Concerning transverse modes $\theta = 0$, the application of the criterion described by equation (2.6) to the point at the centre of the vortices allows one to express the

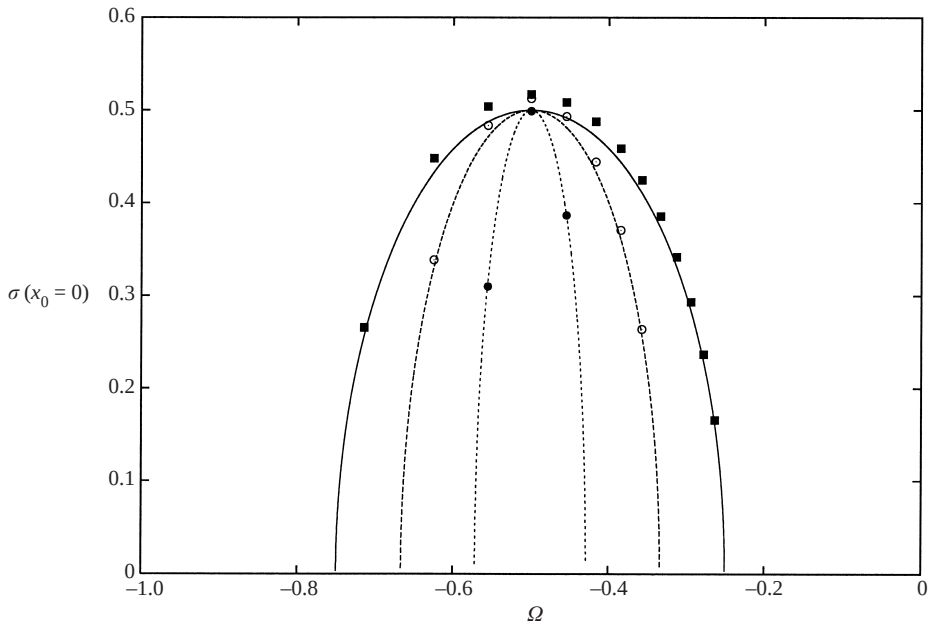

FIGURE 8. Distribution of the Floquet amplification parameter σ for the elliptic instability at the centre of the Stuart vortices, and for spanwise modes at $\theta = 0$, as a function of the rotation rate Ω, according to equation (4.2): ———, $\rho = 1/3$; — — — —, $\rho = 1/2$; and – – – –, $\rho = 3/4$. The symbols indicate the corresponding numerical results obtained from the local stability analysis (squares for $\rho = 1/3$, open circles for $\rho = 1/2$ and black circles for $\rho = 3/4$).

amplification rate as:

$$\sigma(x_0 = 0) = \sqrt{\frac{1}{4} - \left(\frac{1+\rho}{1-\rho}\right)^2 \left(\frac{1}{2} + \frac{1}{Ro}\right)^2}\,, \tag{4.2}$$

with $1/Ro = \Omega(1-\rho)/(1+\rho)$.

The elliptical instability band can then be plotted in terms of Ω-dependence, as done on figure 8 for three values of ρ, along with the predictions from our analysis. The agreement is quite good in the three cases. Note that the amplification factor may be reduced and its maximum shifted for eigenmodes with moderate transverse wavenumbers, as shown by Le Dizès (2000).

4.2. *Case* $\rho = 1/3$

This case with strong ellipticity was thoroughly analysed by Leblanc & Cambon (1998). The values of vorticity and ellipticity at the core are $W_0 = -2$ and $E = 1/\sqrt{\rho} = 1.732$, respectively. Let us begin with the non-rotating case at $Ro = \infty$. A three-dimensional plot of the Floquet parameter is presented as a function of the x_0-coordinate and the angle θ of the wavevector on figure 9(a). It also shows contours of isolevels for this surface, and the variation of the circulation with respect to x_0. (With regard to this Γ_a curve, the scale is arbitrarily chosen, independently of that shown on the vertical σ-axis, as in all the following similar representations.) At $x_0 = 0$, i.e. in the core of the vortex, the trace of the elliptic instability is observed, as plotted on figure 9(b), exactly as in the previously mentioned works by Bayly (1986), Waleffe (1990) and Leblanc & Cambon (1997). The instability peak is located around 0.95 as

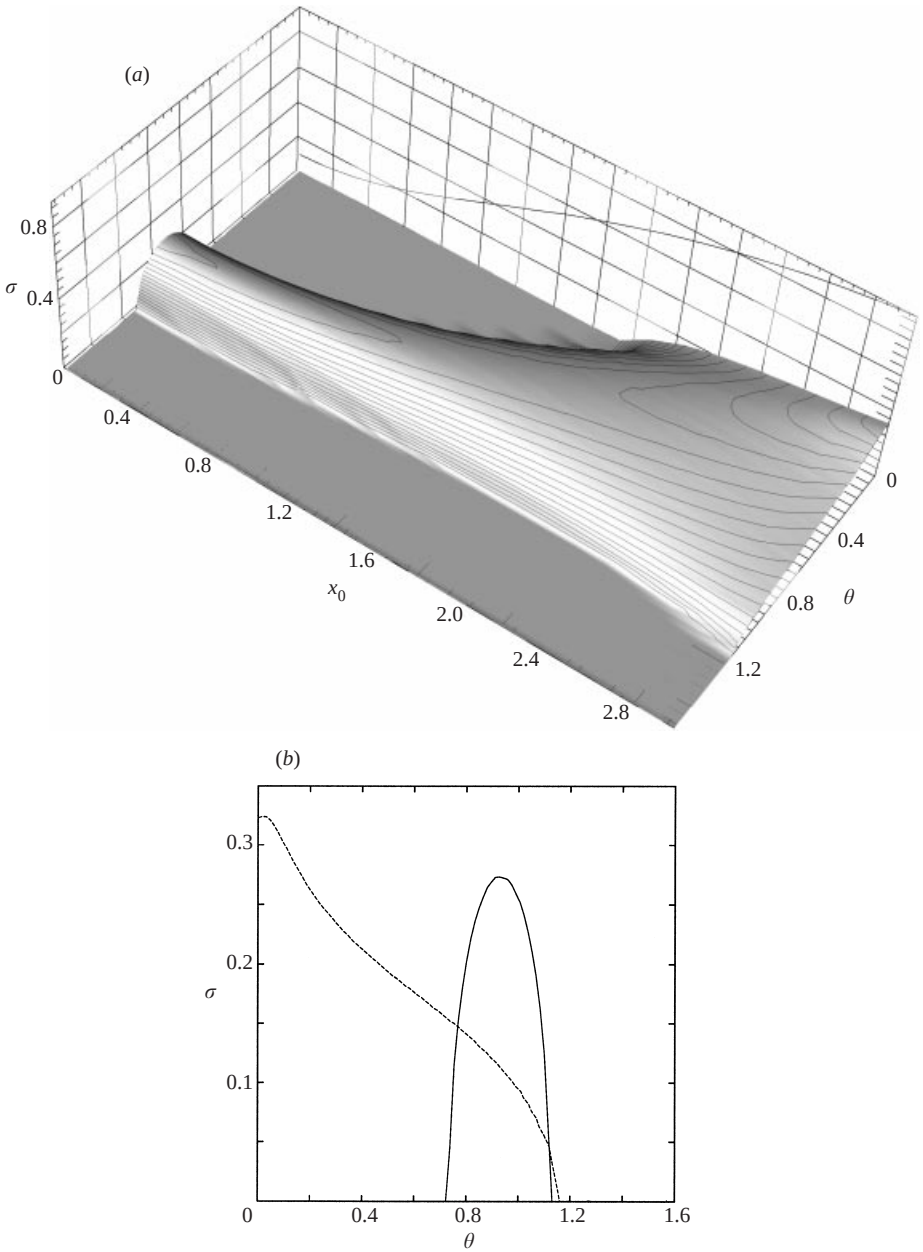

FIGURE 9. $\rho = 1/3$, $Ro = \infty$. (*a*) Floquet amplification parameter σ as a function of the trajectory, indexed by its intersection x_0 with the x-axis, and the orientation θ of the wavevector to the z-axis. (*b*) Slices of the previous three-dimensional plot at $x_0 = 0$ (solid line) and $x_0 = \pi$ (dotted line).

pointed out by Sipp *et al.* (1999), in close agreement with the location at $\theta = \pi/3$ predicted by Cambon (1982) and Bayly (1986).

Returning to the second curve of figure 9(*b*), considering the edge of the Stuart vortex, the most unstable zones are shifted towards smaller θ, and the most unstable wavevector ultimately becomes a pure spanwise mode with $\theta = 0$, at the hyperbolic stagnation point. In the latter case, the growth rate ($\sigma \simeq 0.32$) is slightly larger than for the elliptic mode ($\sigma \simeq 0.27$). Notice also that the evolution of the unstable modes

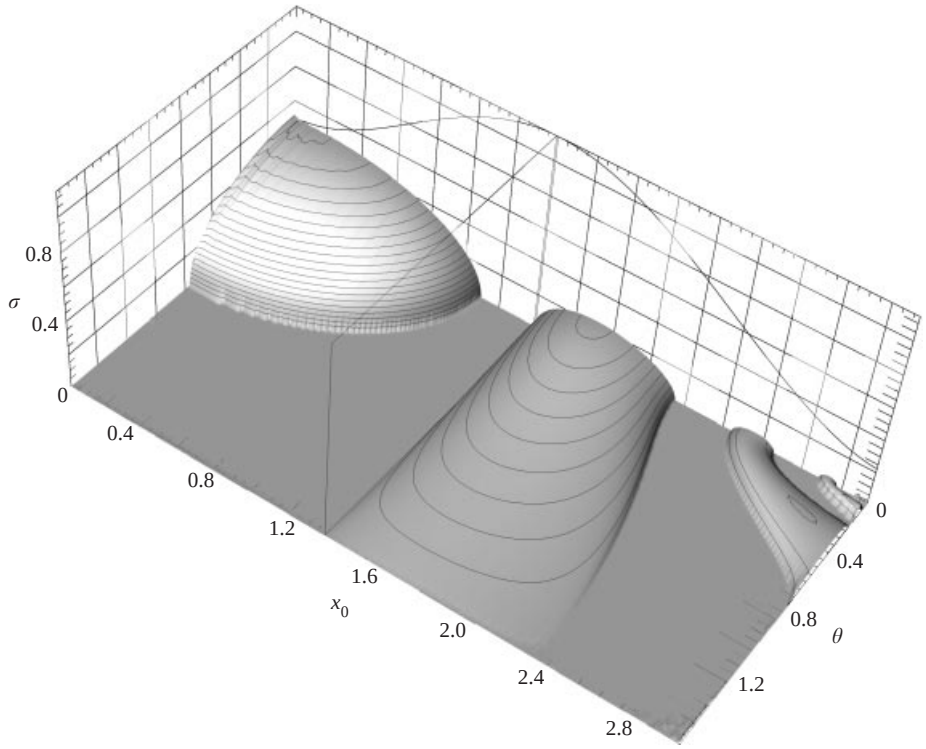

FIGURE 10. Same as figure 9(*a*) but with $\rho = 1/3$ and $Ro = -2$. The absolute circulation, which is a function uniquely of x_0, is traced in the $\theta = 0$ plane, with an arbitrary scale. The contours of a plane through the maximum of Γ_a are also shown, for a convenient observation of the correlation with the position of the band of centrifugal instability.

from the elliptic region to the hyperbolic one happens continuously in this strongly elliptic case.

The rotating case $Ro = -2$, shown on figure 10, is the limit case for maximal destabilization of anticyclones. Three different effects of rotation can be isolated in these results. First, the triggering of a centrifugal instability zone, which did not appear in the previous non-rotating case. As shown on the plot, a broad band of instability appears at intermediate x_0-values in the Floquet parameter surface. Its location is exactly correlated with the x_0-coordinate at which the absolute circulation, computed by (3.22) for the closed *non-circular* streamlines, is minimal, in agreement with the modified Rayleigh criterion of equation (2.2). The unstable domain extends over almost all the θ orientations, but with decreasing amplitude when moving from pure spanwise modes to two-dimensional modes.

Second, the elliptic instability domain is shifted, due to the effect of rotation, towards smaller θ, and finally, values of the Floquet amplification parameters in the hyperbolic region are decreased with respect to the non-rotating case.

Still considering anticyclones, but on the other side of the limiting stable band of figure 1, one sees on figure 11 for $Ro = -1$ that the exact compensation of the Stuart vortex core vorticity by solid body rotation completely annihilates both the elliptic instability and the previously observed centrifugal one. We also observe the emergence of a number of discrete bands of instability near the hyperbolic region, but with small growth rate.

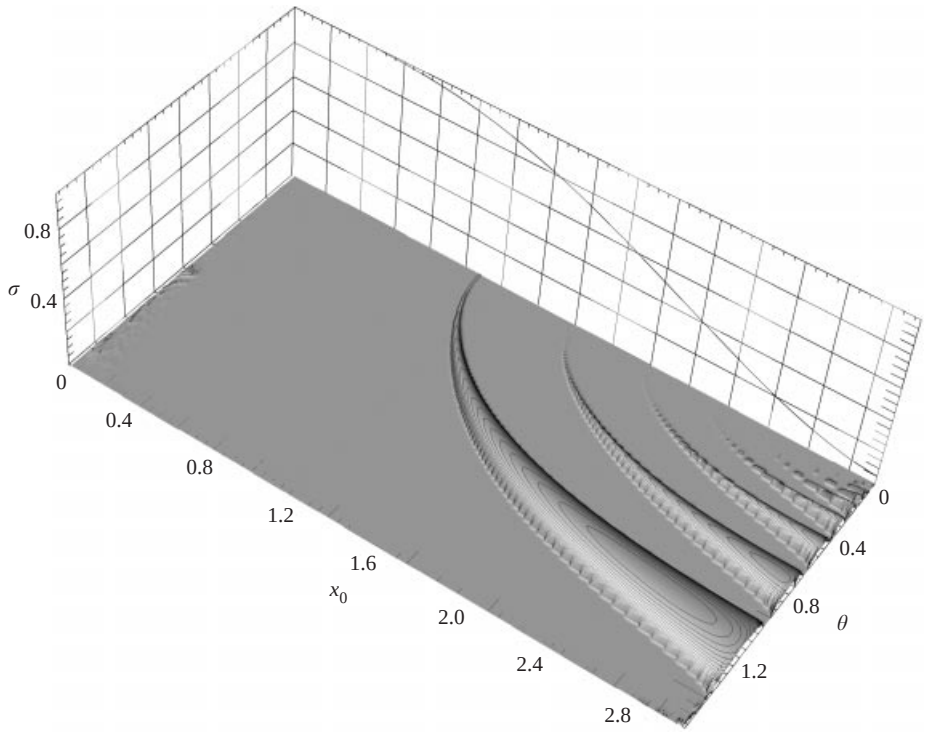

FIGURE 11. Same as figure 9(*a*) but with $\rho = 1/3$ and $Ro = -1$.

4.3. *Case* $\rho = 3/4$

This case was considered by Potylitsin & Peltier (1999), as weakly elliptic. The values of vorticity and ellipticity at the core are $W_0 = -7$ and $E = 1.155$, respectively.

For the non-rotating case, figure 12 shows the characteristic surface of the Floquet parameter dependence in the (x_0,θ)-space. The instability band in the elliptic core is narrower than for the strongly elliptic vortex at $\rho = 1/3$. Here again, unstable modes evolve in a continuous manner when moving to the hyperbolic region, with similar growth rates as observed on figure 9, the maximal one being obtained at $x_0 = \pi^-$.

When the destabilization of anti-cyclonic vortices is maximal, at $Ro = -2$ as shown on figure 13, the unstable band due to the centrifugal modes is quite narrow, and appears as expected at the location of extremal absolute circulation, in that case quite close to the core of the vortex. The growth rate of the centrifugal modes becomes twice as large as the growth rates of the instabilities in the preceding cases. Owing to the weaker ellipticity than in the $\rho = 1/3$ case, the elliptically unstable mode is damped, and confined to a very small core region of spanwise direction. The hyperbolic instability region is, in this case, close to non-existent.

The same tendencies are observed when decreasing the rotation rate, and at $Ro = -5$ the centrifugal instability appears on figure 14 to be pulled away from the centre region, with a larger extent in x_0 than in the previous case. At these values of the geometrical and kinematic parameters, anti-cyclonic Stuart vortices are seen to undergo a very strong three-dimensional destabilization mainly from the centrifugal instability.

At an even smaller value of the rotation rate ($Ro = -14$), shown on figure 15, the

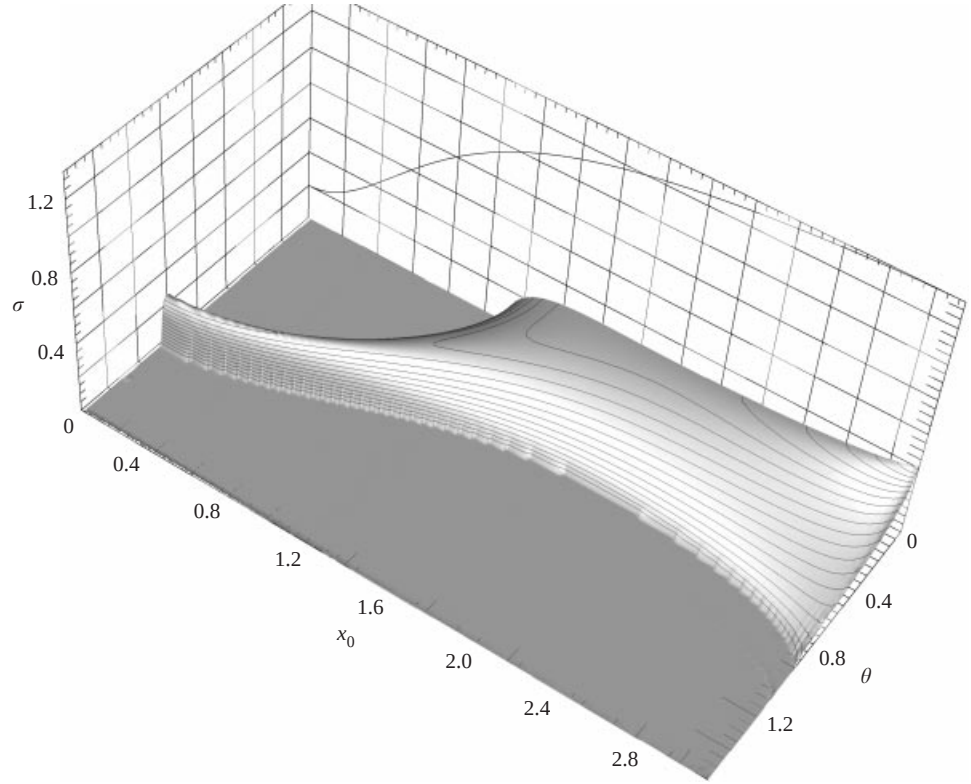

FIGURE 12. Same as figure 9(*a*) but with $\rho = 3/4$ and $Ro = \infty$.

centrifugal instability band is both shifted farther away from the centre and widened, so that it merges with the region in which the hyperbolic instability arises.

4.4. *Case* $\rho = 19/21$

This case is close to the point concentration of vorticity, with $W_0 = -20$ and $E = 1.05$ at the core. The ellipticity is therefore very weak.

Accordingly, the map of the Floquet parameter (shown on figure 16) is slightly different than in the other two non-rotating cases. Since ellipticity is weak, so is the influence of the elliptic mode of instability away from the centre: no such unstable mode is found for values of x_0 larger than 1, say. In that case, the hyperbolic instability zone emerges by itself on the stability diagram, clearly separated from the other unstable zone, and observed to be confined to a quite small part of the (x_0,θ) parameter space.

4.5. *Case* $\rho = 1$

This case is special since it corresponds to an irrotational flow in the rotating frame of reference: the relative vorticity vanishes everywhere, except on the core of the vortices, where it is infinite. The relative circulation of each point vortex remains -4π.

Without background rotation, it may be shown that any open or closed streamline (except the hyperbolic stagnation point) is stable with respect to exponentially growing short-wavelength perturbations (see Appendix B). Algebraic growth may occur. Neither elliptic nor centrifugal instability occurs. The only exponential instability is concentrated on the hyperbolic stagnation point, which is unstable.

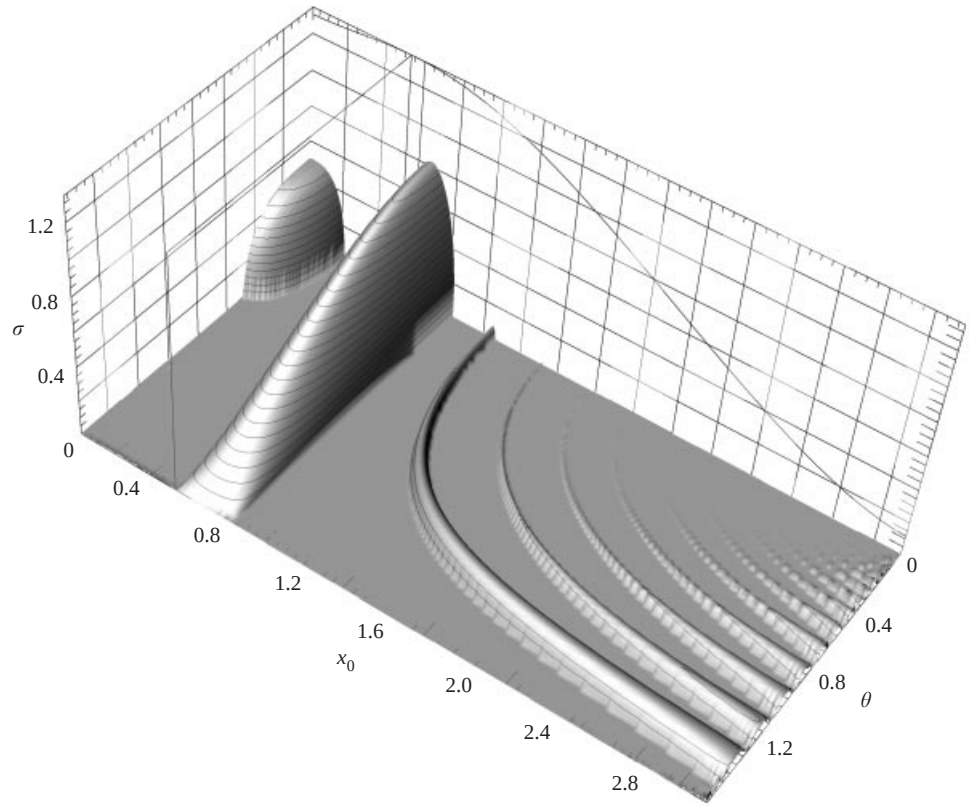

FIGURE 13. Same as figure 9(*a*) but for the anticyclonic case $Ro = -2$ with $\rho = 3/4$.

Under rotation, this latter hyperbolic instability persists, and centrifugal instability is expected. Indeed, for a pure circular potential vortex ($W(r) = 0$ and $U(r) \sim r^{-1}$), the sufficient condition for instability $\Phi(r) < 0$ with $\Phi(r)$ given by (2.2) is easily shown to be fulfilled somewhere for any rotation rate. For flows with non-circular streamlines, such as the Stuart vortices, the Sipp–Jacquin criterion (equation (5.2)) is thus expected to hold.

4.6. *Open trajectories*

The evolution of the amplification parameter in the (θ,y_0)-space is plotted for the non-rotating case on figure 17 and on figure 18 for the anticyclonic case $Ro = -5$. We observe that on following the open trajectories remnants of the hyperbolic instability appear, with an amplification that quickly vanishes with increasing y_0, especially in the strong anticyclonic case of figure 18. However with respect to the non-rotating case, the maximal amplification value of about 0.35 is the same, obtained for the spanwise $\theta = 0$ mode.

5. Synthesis of the instability criteria

In the following, we summarize the instability results, aiming at providing precise – and, we hope, as definitive as possible – answers to the problem of linear stability of two-dimensional vortex flows in a rotating frame.

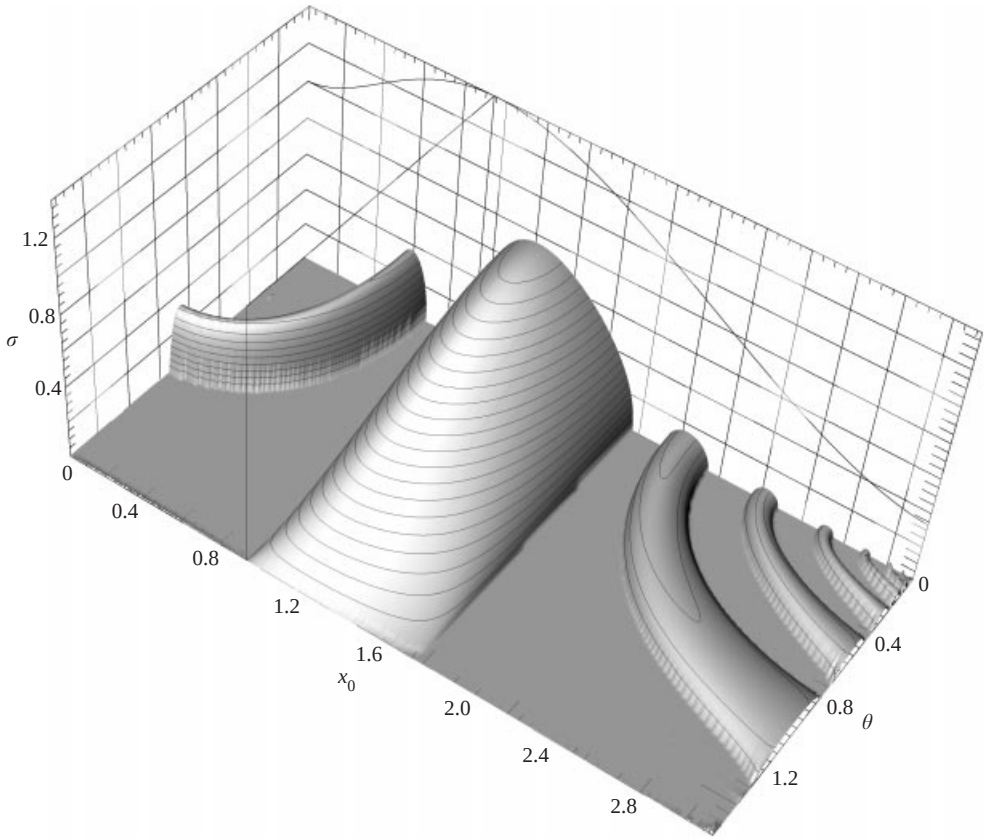

FIGURE 14. Same as figure 9(*a*) but for the anticyclonic case $Ro = -5$, with $\rho = 3/4$.

5.1. *Results on the three background instabilities*

The geometrical optics method allowed us to apply zonal RDT equations along individual streamlines for short-wavelength disturbances. Some simple mechanisms identified in simplified extensional flow given by (3.3) and (3.5), in a rotating frame, were retrieved in more complex flows, such as the Taylor–Green and the Stuart vortices. Local analysis is invaluable for substituting the *informative* taxonomy of unstable modes, *hyperbolic, elliptic, centrifugal*, to the *zoological* one, *braid, core, edge*, initially used by Peltier and coworkers (see e.g. Smyth & Peltier 1994).

As shown in figures 10, 12, 13, 14 and 16 the elliptic mode is captured as an oblique mode whose angular location θ and amplification rate σ is found for individual streamlines near the core, in a way consistent with previous RDT and stability analyses for extensional flows (Cambon 1982; Bayly 1986; Cambon *et al.* 1994). The relevance of equations (2.3) and (2.4) is confirmed for predicting the shift in the angular location θ of the most amplified mode, and the modification of its amplification rate by system rotation. In particular, the elliptic mode, which is located at $\theta \sim \pi/3$ with no rotation, is shifted towards a spanwise mode $\theta \sim 0$ and is more amplified in the anticyclonic case, in agreement with a maximum amplification for $Ro = -2$ (figure 19). These results are also consistent with the ones of Sipp and coworkers for the rectangular Taylor–Green vortices with small aspect ratio, and to the results of Le Dizès (2000) for vortices in a weak external rotating strain field.

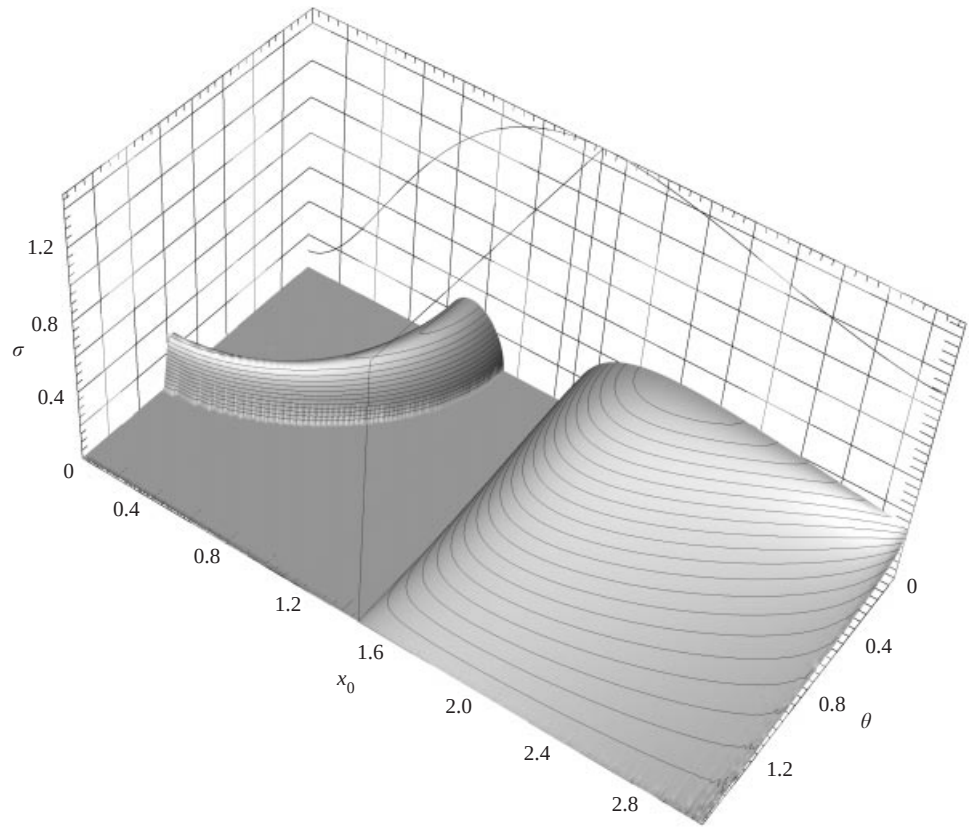

FIGURE 15. Same as figure 9(*a*) but for the anticyclonic case $Ro = -14$, with $\rho = 3/4$.

The identification of the centrifugal mode in the anticyclonic cases ($Ro < 0$) is also clear and accurate using the local analysis along intermediate streamlines between the core and the periphery. This mode is confirmed to be essentially spanwise ($\theta = 0$), and inwardly bounded by the streamline where the absolute circulation reaches a maximum. This characteristic streamline moves towards the periphery of the Stuart vortices as the anticyclonic system rotation gets smaller and smaller, so that the centrifugal and the hyperbolic modes can eventually merge.

It is confirmed that the unstable hyperbolic mode is essentially spanwise ($\theta = 0$), located near peripheral streamlines, and cancelled by a large enough rotation rate. Recall that on the hyperbolic stagnation point itself, it may be shown that when it is rotational (which is the case when $\rho \neq 1$), its stability property is asymmetric with respect to the rotation rate (see figure 4), i.e. anticyclonic rotations are more destabilizing than cyclonic ones. The corresponding growth rate may be expressed explicitly (see details in Leblanc 1997).

The most important result illustrated by figures 10, 13 and 14 is the competition between centrifugal and elliptic instabilities in the anticyclonic case. For values of the Rossby number around $Ro = -2$, where both instability modes are important, the elliptic instability is shown to be dominant for the lowest value of ρ. Of course, centrifugal instability is dominant for the cases with weaker core ellipticity. Finally, the centrifugal instability explains the asymmetry of the effect of system rotation and destabilization of anticyclonic vortices for quasi-circular vortices, whereas this

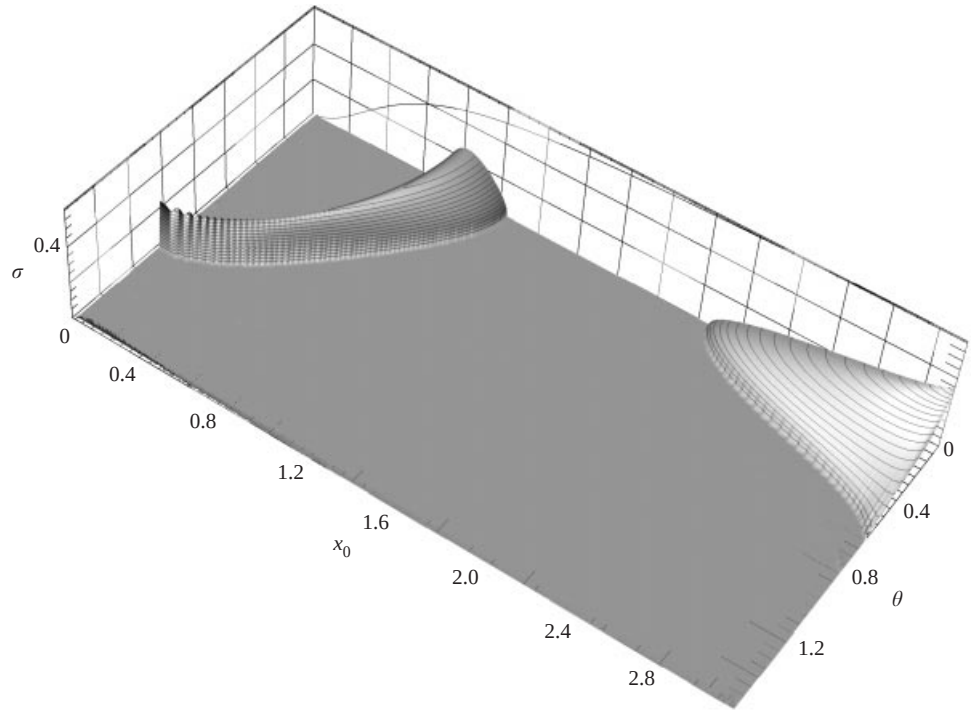

FIGURE 16. Same as figure 9(*a*) but with $\rho = 19/21$ and $Ro = \infty$.

explanation is provided by the elliptic instability if the core of the vortex is elliptic enough. A quantitative study of the domain (ρ, ψ, Ro) in which the influence of the centrifugal instability is relevant, was recently proposed by Sipp & Jacquin (2000), but in connection with local criteria for spanwise modes of disturbances only (see § 5.2 below).

Finally, note that any streamline (except the hyperbolic point) at zero absolute vorticity $W(x_0)+2\Omega = 0$ may be shown to be stable to short-wavelength perturbations (see Appendix B). This extends the now classical result of 'gyroscopic stabilization' of the elliptical instability in a rotating frame (Craik 1989; Cambon *et al.* 1994; Bayly *et al.* 1996; Leblanc 1997).

5.2. *Validity of criteria obtained with pure spanwise perturbations*

Although the basic elliptical instability involves oblique modes at $\theta \sim \pi/3$ – so that spanwise modes ($\theta = 0$) are stable without rotation – in the rotating case, maximum amplification is found at $Ro = -2$, again for a spanwise mode. Hence, the special case of spanwise modes which are naturally unaffected by pressure disturbances requires particular attention. Short-wave dynamics is simplified for these modes since the $k_i k_j/k^2$ factors disappear from the last equation of (3.18). Leblanc & Cambon (1997) proposed generalizing the inertial discriminant, which reduces to (2.6) in the case of an extensional flow, using the form

$$\Phi_{LC} = 2(\Omega + U/\mathscr{R})(W + 2\Omega) - (\partial_s U)^2 \tag{5.1}$$

where Φ_{LC} is the determinant of the inertial matrix in curvilinear coordinates (s, ψ), with s the curvilinear abscissa, $\mathscr{R}$ the local curvature radius, $U = \mathrm{d}s/\mathrm{d}t$ the velocity amplitude, and $W = -\nabla^2\psi$ the modulus of vorticity at the given streamline. In the

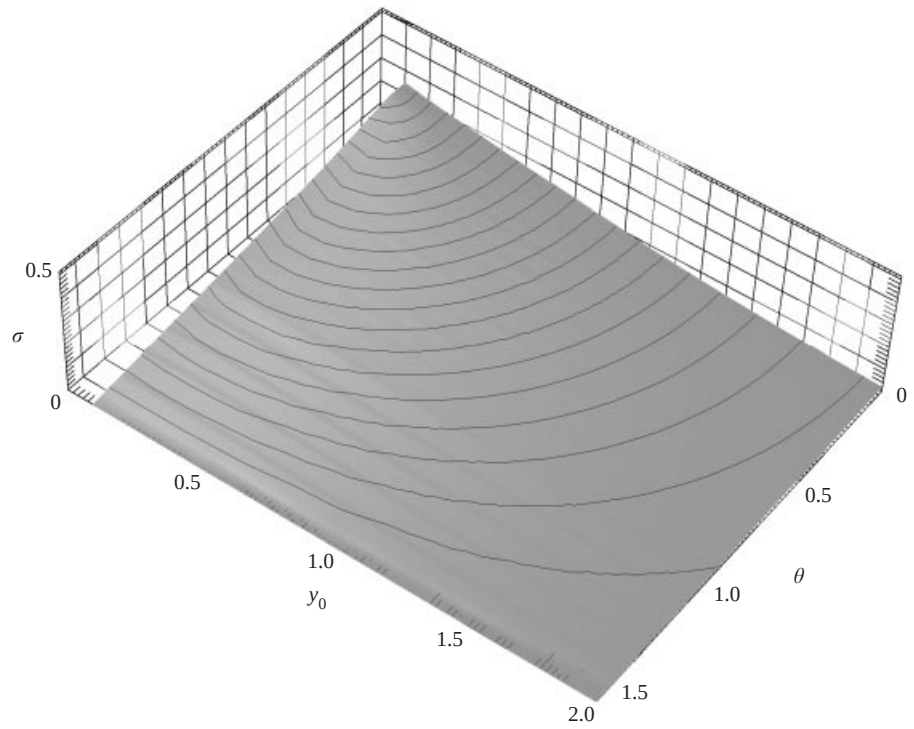

FIGURE 17. Distribution of the amplification parameter σ with respect to the y_0-coordinate at $x = 0$ for the open trajectories, at $Ro = \infty$.

particular case of centrifugal instabilities, Sipp & Jacquin (2000) showed that the right criterion is

$$\Phi_{SJ} = 2(\Omega + U/\mathscr{R})(W + 2\Omega) \tag{5.2}$$

instead, generalizing the result of Bayly (1988), so that $\Phi < 0$ on a whole trajectory is a sufficient condition for having a centrifugal instability. Introducing the intrinsic shear rate (or shear vorticity) $\mathscr{S}_h$ defined from $W = -2\mathscr{S}_h + 2U/\mathscr{R}$ (note that, in the limiting case of a parallel flow, the shear obtained from this definition is half that of the commonly used shear parameter), equation (5.2) becomes $\Phi_{SJ} = (W + 2\Omega + 2\mathscr{S}_h)(W + 2\Omega)$, or, equivalently $\Phi_{SJ} = -(\mathscr{S}_h)^2 + (W + 2\Omega + \mathscr{S}_h)^2$. The criterion (5.1) differs from (5.2) through the diagonal contribution $\partial_s U$ to the strain rate in the inertial tensor. Note that in the general case in which the matrix of the linear system of equations is time-dependent over a streamline, stability is not necessarily determined by the determinant of this matrix. In the analysis of Sipp & Jacquin, the pressureless system (3.18) is projected onto a special basis, so that its matrix becomes triangular and its determinant does characterize the stability; this matrix differs from the inertial tensor from the term $\partial_s U$.

A significant difference can be found when comparing the *local* Rossby numbers which give the maximum destabilization for elliptic and centrifugal instability. When the elliptic instability is involved, the maximum destabilization is found near the Rossby number $Ro = -2$, and a significant range of Rossby numbers around $Ro = -1$, the case of zero absolute vorticity, yields stability. This is consistent with results obtained from the analysis at vanishing ellipticity, which predicts stability for $-2/3 > Ro > -2$, and instability with amplification rate (2.4) outside this domain. In the

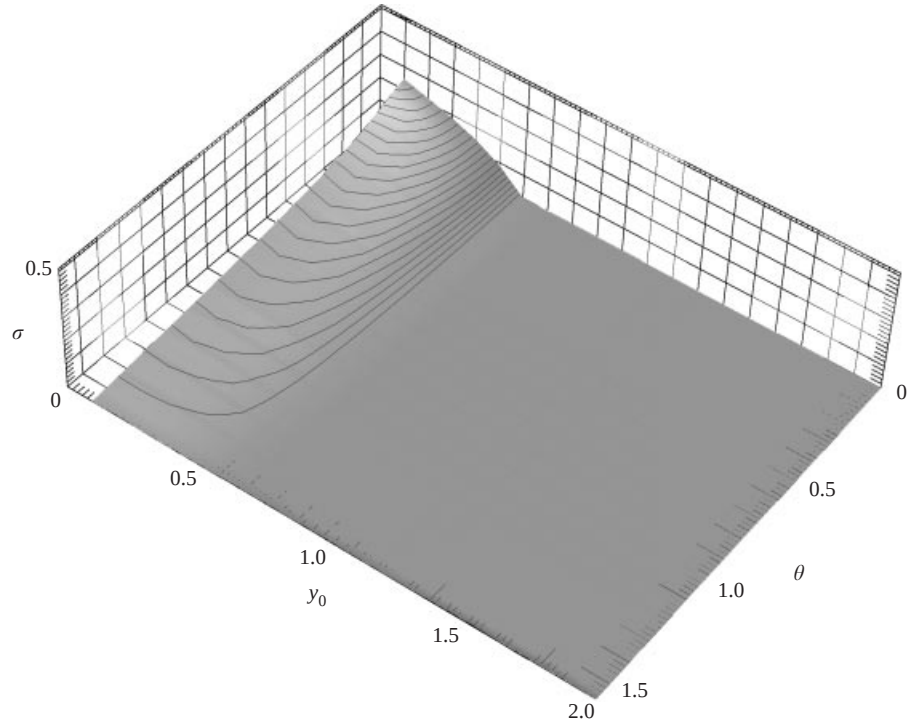

FIGURE 18. Same as figure 17 but for the anticyclonic case $Ro = -5$.

elliptic case, the choice of the vorticity at the core for defining the Rossby number is convenient, without need of an alternative. The situation is rather different when the centrifugal instability is involved, since it may appear on an intermediate range of streamlines, not necessarily close to the core, so that the local vorticity may change and get smaller in absolute value from the core vorticity. Results of figures 10, 13 and 14 show that the centrifugal instability takes place for streamlines nearly outward from the streamline where the absolute circulation has a maximum. It is easy to show that this limiting streamline corresponds to a change of sign of the absolute vorticity (Appendix A), in agreement with the generalization of Kloosterziel's criterion (Kloosterziel & van Heijst 1991) to non-circular streamlines, and with the analysis of Sipp & Jacquin (1998). Accordingly, the centrifugal instability occurs over an annulus of streamlines, whose local Rossby number Ro_ψ is in the range $0 > Ro_\psi > -1$. Hence the domain of maximum amplification of elliptic instability by system rotation, and the domain of activation of centrifugal instability by rotation as well, involve different ranges of Rossby numbers, assuming these are defined locally.

6. Conclusion

In this work, we have shown that the 'local method' can predict the three fundamental instabilities, of hyperbolic (H), elliptical (E) and centrifugal (C) types, the features of which are closely related to those of canonical flows of reference.

The hyperbolic instability appears to be weakly sensitive to the cyclonic–anticyclonic asymmetry, and to be inhibited by rotation, at a high enough rate. Surprisingly, this

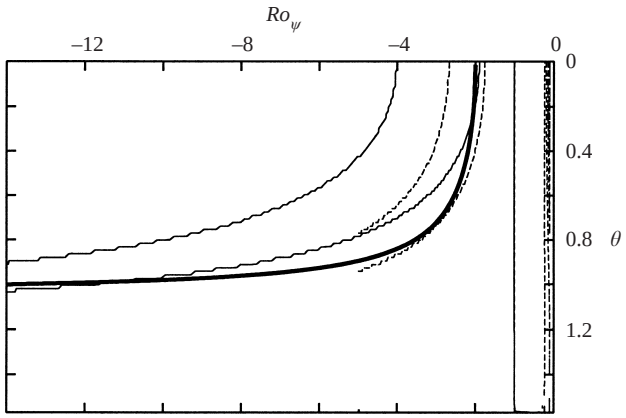

FIGURE 19. Boundaries of the unstable zones in the plane (Ro_ψ,θ), for $\rho = 3/4$ and $Ro = -14$ (solid line) and $Ro = -5$ (dashes). The heavy solid line indicates the analytical prediction obtained from equation (2.3) for the elliptical instability. The centrifugal instability bands are bounded on the left by the $Ro_\psi = -1$ value.

instability does not seem to have been found by Sipp in a flow consisting of Taylor–Green vortices at $\Omega = 0$ (Sipp & Jacquin 1998; Sipp *et al.* 1999).

For the characterization of the elliptical instability by the local method, Sipp & Jacquin (1998) used general disturbance orientations θ only in the $\Omega = 0$ case, again for the Taylor–Green cell flow. They restricted the more general $\Omega \neq 0$ analysis to the particular orientation $\theta = 0$. In the present study, we show that this method is able to lock onto the angular peak of elliptic instability, and follow its shifting by rotation.

Very close to the core ($x_0 = 0$), the values of θ_{peak} and σ_{max} in our results fit very well the theoretical predictions of equations (2.3) and (4.1), as shown in figure 19. Maximal amplification is shown at $Ro = -2$, with $\sigma_{max} \simeq S = 1/2$ and $\theta_{peak} \simeq 0$ (figures 10, 13), whereas $\theta_{peak} \simeq \pi/3$, $\sigma_{max} \simeq 9S/16$ is recovered without rotation (figures 9*a*, 12, 16). Different tendencies occur outside the core when looking at figures 12, 14, 15, 16: clearly, an elliptical instability branch emanates from the core. Without rotation (see e.g. figure 16), the fact that θ_{peak} decreases outward from the core may be partially explained by an increasing ellipticity (see the semi-analytical result on curve (*b*) of figure 1 in the paper by Bayly 1986). On the other hand, the decrease with $W(\Psi)$ of the local Rossby number in absolute value would lead to decreasing θ_{peak} according to the anticyclonic branch $-\infty > Ro > -2$ of equation (2.3). As shown on figure 19, equation (2.3) remains relevant in correctly predicting the dependence of θ upon Ro close to the outer boundary of the elliptic branch rather than its crest. In terms of local anticyclonic Rossby numbers, the elliptical branches of figures 14 and 15 are in the intervals $[-5,-2]$ and $[-14,-2]$ respectively. In the cyclonic case (figure 20), the location of the elliptical instability branch at the core $x_0 = 0$ agrees with the value computed from equation (2.3).

For the centrifugal instability, our study confirms its triggering in the non-circular case, and provides the inner limiting bound of its domain of existence as being the trajectory at which maximal absolute circulation is attained. This condition also amounts to zeroing the absolute vorticity. For the case of rotating Taylor–Green vortices studied by means of a normal-mode analysis, Sipp & Jacquin (2000) agree with this criterion. On the other hand, the numerical simulations by Potylitsin & Peltier 1999 are performed at too low values of k_3, preventing one to distinguish one

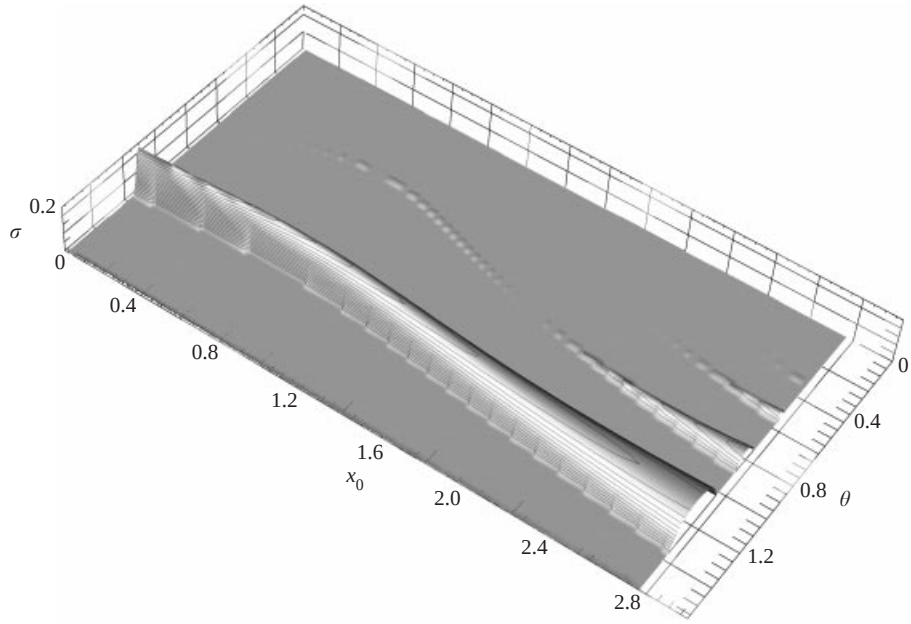

FIGURE 20. Same as figure 9(*a*) but with $\rho = 3/4$ in the cyclonic case $Ro = 5$.

kind of instability from another, and as a consequence to make sure that their 'edge' modes are actual centrifugal ones, in the absence of additional theoretical evidence. The simulations of Kelvin–Helmholtz vortices by these same authors (Potylitsin & Peltier 1998) exhibit a more convincing centrifugal instability character, from the 'torus'-like shape of the observed modes.

In order to explain the preferential destabilization of anticyclones with respect to cyclones, only the elliptical and centrifugal instabilities remain good candidates among the initial three ones. From equation (2.4), one identifies two branches of elliptical instability. One yields strong amplification for anticyclones in the interval $Ro \in]-\infty, -2[$, this main branch being clearly observed on figures 14 and 15, with maximum amplification around $Ro = -2$ for transverse modes. The second branch for $Ro \in]-2/3, 0[$ also extends for $Ro > 0$ to destabilize cyclonic vortices, with smaller amplification rates of oblique modes. This latter branch may eventually collide the (C) instability domain.

The main branch of (E) and the (C) instabilities take place in non-overlapping intervals of the local Rossby number $Ro_\psi = W(\psi)/(2\Omega)$, as in the sketch in figure 21, partly suggested by Sipp (private communication). Let us begin by considering a given trajectory $\psi =$ constant along which the vorticity is $W(\psi)$, and by letting the frame vorticity 2Ω vary. Bearing in mind that $W < 0$ and $\mathscr{R} < 0$, we see on figure 21 that the centrifugal instability domain lies on the right of the always stable limit of zero absolute vorticity, i.e. $2\Omega = -W$ or equivalently $Ro_\psi = -1$. The elliptical instability main branch domain lies systematically on the left of this $Ro_\psi = -1$ limit, from which it is separated by an always stable region. Built on grounds of pressureless modes ($\theta = 0$), criteria such as Φ_{SJ}, Φ and Φ_{LC} suggest $2\mathscr{S}_h$ and $2S$ as respective width scales for the (C) and (E) zones in our picture. Figure 23 quantitatively supports this argument, with the additional careful note that the (E) domain is no longer centred around $Ro_\psi = -2$ on this plot, when the (E) band approaches the periphery of the vortex. The largest amplification seems to keep the $Ro_\psi = -2$ value though.

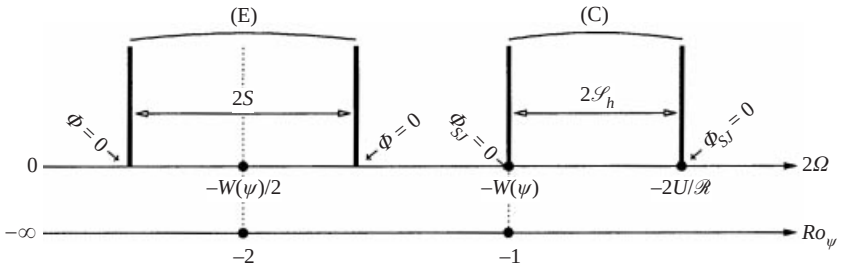

FIGURE 21. Sketch of the (E) and (C) instabilities (partly suggested by Sipp, personal communication).

Focusing on the many criteria for pressureless modes, the following statements can be made:

(i) The criterion $\Phi = -S^2 + (2\Omega + W_0/2)^2$ (equation (2.6)) suggests the (E) part of our scheme, but is restricted to the canonical 'extensional' flow, and additionally is probably restricted to a neighbourhood of stagnation points. The limits of the (E) band are at the $\Phi = 0$ locations, with negative Φ in between.

(ii) The criterion $\Phi_{SJ} = -\mathscr{S}_h^2 + (W + 2\Omega + \mathscr{S}_h)^2$ (equation (5.2)) departs from the latter by $-(\partial U/\partial s)^2$, where $S^2 = \mathscr{S}_h^2 + (\partial U/\partial s)^2$ (Appendix A). Φ_{SJ} is valid for the centrifugal instability, but not with certainty for the other kinds of instability. It however is useful for the (C) part of our diagram, since $\Phi_{SJ} = 0$ on the limits of the (C) band, and is negative in between.

Although Φ_{SJ} exhibits extrema at a value of Ro_ψ which is expressed identically as $Ro = -1 - \mathscr{S}_h/(2\Omega)$ in terms of $\mathscr{S}_h$, one has to be aware that $\mathscr{S}_h$ itself is expressed differently in each case. Consequently, the centrifugal instability region given in Ro_ψ-space is very different from that of the (E) and (H) ones, even in the pure parallel shear case.† Within the unstable centrifugal instability zone, $0 > Ro_\psi > -1$, $\mathscr{S}_h < 0$ and the absolute vorticity is cyclonic. For the other instabilities, $Ro_\psi < -1$ in their sphere of action, and the absolute vorticity is anticyclonic ($\mathscr{S}_h > 0$).

An ever-present difference between centrifugal destabilization and the others comes from the presence of the curvature term in $\mathscr{S}_h = -W/2 + U/\mathscr{R}$. In the other instabilities, the vorticity term is leading so that $\mathscr{S}_h > 0$ with $W < 0$, whereas $U/\mathscr{R}$ is dominant in the unstable centrifugal zone, with $\mathscr{S}_h < 0$ and $U/\mathscr{R} < 0$ (see the sign map of $\mathscr{S}_h$ for $\rho = 3/4$ on figure 22). Therefore, destabilization of anticyclones comes from either the centrifugal instability for $Ro_\psi \simeq -0.5$, or the elliptical instability for $Ro_\psi \simeq -2$.

The question remains open however as to whether an actual flow such as the mixing layer can be interpreted in as simple terms. Indeed, the outcome of the competition between the remaining two candidate instabilities depends in a dramatic way upon the ellipticity. This translates into the value of ρ for the Stuart vortices as shown on figure 23: at small ρ (E) defeats (C), and vice versa at large ρ.

Let us now conclude our work with a discussion about possible extensions and limits of the geometric optics stability theory. First, it is worth mentioning that short-wavelength linear instabilities may be extended to the nonlinear regime in a relatively straightforward way when the amplitude of the WKB disturbance (3.10) scales with ϵ (Lifschitz 1991). In that case, it may be shown that the evolution of the corresponding

† Normal-mode analysis for $\rho = 0$ with rotation produces maximal destabilization at $W/(2\Omega) = -(\partial U_1/\partial x_2)/(2\Omega) \simeq -2.5$, fully in agreement with the Φ criterion (Yanase *et al.* 1993). See also figure 4 in Leblanc & Cambon (1997).

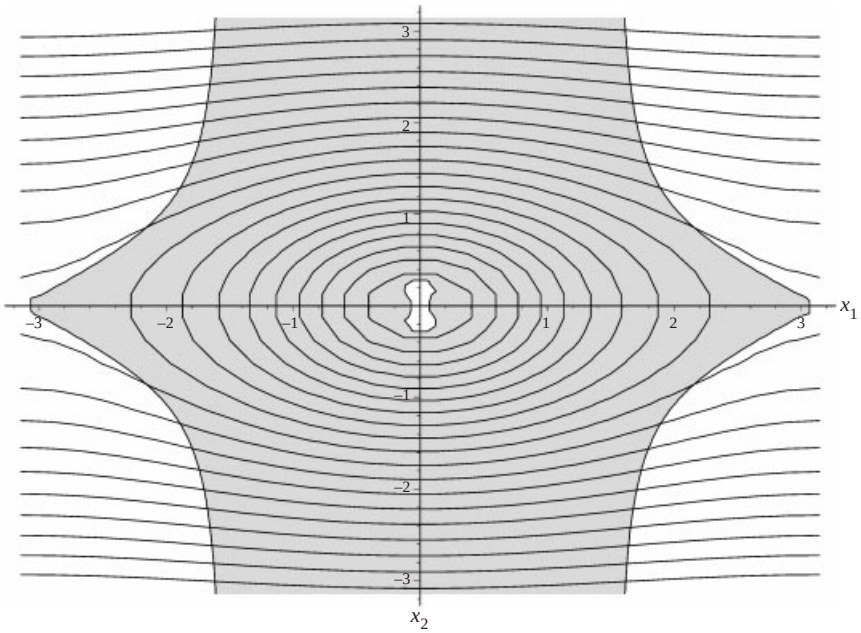

FIGURE 22. Map in the (x_1, x_2)-plane of the negative zones of $\mathscr{S}_h$ (shaded area) and of its domain of positiveness (white areas). Streamlines of the Stuart vortex flow are shown for the same parameter, $\rho = 3/4$. It is clear that, along streamlines around the elliptical or hyperbolic stagnation points, $\mathscr{S}_h$ changes sign, whereas in the intermediate region where centrifugal instability may occur, its sign is constant and negative.

weakly nonlinear disturbance is governed by the same system of ODEs as in the linear case, i.e. (3.18). Following the terminology of nonlinear geometric optics, this means that *vorticity waves are linearly degenerate*, a well known fact in compressible flows (see for instance Majda 1984). As proved by Lifschitz (1991), and provided the wave vector is bounded, linear instability is equivalent to the nonlinear growth of the vorticity disturbance.

Furthermore, two of the advantages of the local method are its small cost in numerical resources, and the fact that it can help suggest semi-analytical criteria. It seems that the fundamental underlying assumptions associated with it do not prevent it from comparing well with normal-mode analyses, where the latter are available (Leblanc & Cambon 1998; Sipp & Jacquin 1998; Sipp *et al.* 1999; Sipp & Jacquin 2000), of course at sufficiently high k_3.

Although the link between geometric optics theory and normal-mode methods (associated respectively with the continuous and the discrete parts of the spectrum) remains to be clarified in the general case, interesting progress has been made in this direction. At first, Bayly's construction of centrifugal modes (Bayly 1988) gives a correction to the WKB growth rate which is in remarkable agreement with normal-mode computations (see Sipp *et al.* 1999; Le Duc & Leblanc 1999). More recently, Le Dizès (2000) gave the correction to the WKB growth rate in the case of a Rankine vortex in a multipolar strain field, including the elliptical instability in a rotating frame which is of interest here. Briefly, this correction requires knowledge of the dispersion relation for the linear problem, which is indeed the case for the Rankine vortex. For more complex flows, such as Stuart vortices, the dispersion relation cannot be obtained in explicit form, and a similar construction of normal modes is

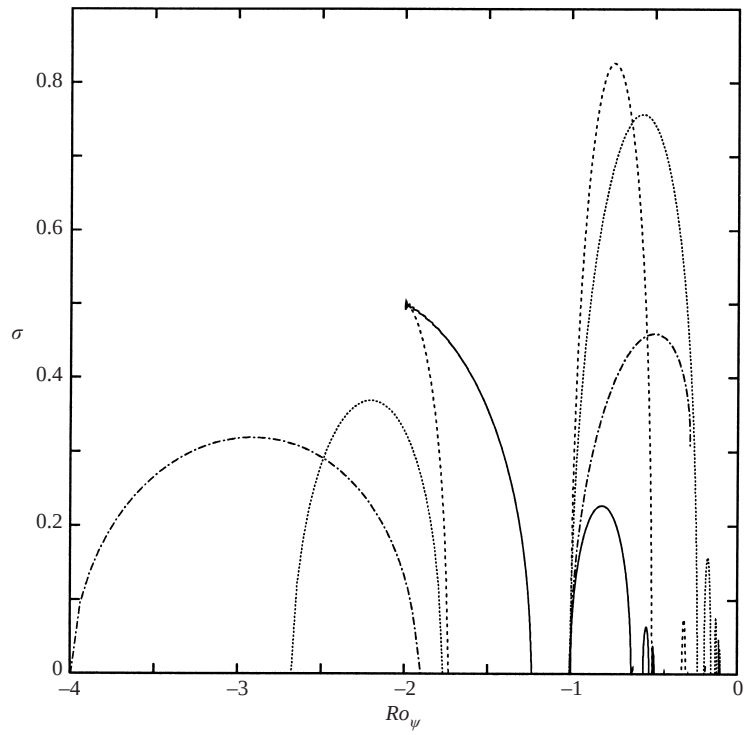

FIGURE 23. Distribution of the Floquet amplification parameter σ for spanwise modes at $\theta = 0$, as a function of the local Rossby number Ro_ψ. ———, $\rho = 1/3$, and core Rossby number $Ro = -2$; — — — —, $\rho = 1/3$ at $Ro = -1$; - - - -, $\rho = 3/4$, $Ro = -2$; - - - -, $\rho = 3/4$, $Ro = -5$; — · — · —, $\rho = 3/4$, $Ro = -14$. The centrifugally unstable band lies on the right of $Ro_\psi = -1$, and the elliptical instability band is on the left of this value, from which it is separated by a stable zone.

therefore impossible to achieve. However, Le Dizes proposed a heuristic scheme for computing the growth rate of normal modes with moderate wavenumbers k_3, from results obtained with geometric optics. Although this correction agrees fairly well with normal-mode calculations, it cannot be computed without knowledge of one particular value of the normal-mode growth rate. However, this requires picking a result from an eigenmode computation (a rather difficult problem for flows like Stuart vortices, see e.g. Pierrehumbert & Widnall 1982; Leblanc & Cambon 1998; Potylitsin & Peltier 1999).

Of course, geometric optics also has limits, as we would like now to illustrate. The analysis proposed by Lifschitz & Hameiri (1991), and homogeneous RDT, can in principle account for algebraic growth, since they essentially provide solutions to initial value problems. However, Floquet analysis is restricted to exponential growth – of the disturbance field amplitude $\boldsymbol{a}$. This analysis is correct if and only if the evolution of the disturbance wavevector is periodic, amounting to the strict condition $\boldsymbol{k} \cdot \boldsymbol{U} = 0$, but for those particular flows where $\mathrm{d}T/\mathrm{d}\psi = 0$ (as shown in Appendices A and B). The more general case $\boldsymbol{k} \cdot \boldsymbol{U} \neq 0$ can hardly be overlooked on the mere argument of viscous cut-off (Sipp & Jacquin 1998), but should be dealt with in future works, as an extension of the present study.

More specifically, the problem of non-uniform convergence of the general case toward the specialized cases characterized by $\boldsymbol{k} \cdot \boldsymbol{U} = 0$ or $\mathrm{d}T/\mathrm{d}\psi = 0$ deserves special attention. If $\boldsymbol{k} \cdot \boldsymbol{U} \neq 0$ and $\mathrm{d}T/\mathrm{d}\psi \neq 0$, the disturbance wavevector $\boldsymbol{k}$ tends

asymptotically, i.e. after a large number of periods, to be aligned with the direction of $\nabla\psi$, and with an increasing modulus. In that case, the analysis of the Kelvin–Townsend equations should be extended over a larger integrating time. In the limit $\mathrm{d}T/\mathrm{d}\psi \to 0$, e.g. in a neighbourhood of the elliptical point, the theory might have to be adapted for including higher-order terms in the ϵ-development of equation (3.10).

The authors would like to thank Dr Denis Sipp for providing a skeleton of the code used in numerical computations, and for discussions about the theory. S. L. is grateful to Pierre Seppecher for fruitful discussions on differential geometry. C. C. wishes to acknowledge support from the Isaac Newton Institute, Cambridge, UK, during the 1999 Turbulence Programme.

Appendix A. Intrinsic shear rate, curvature, and other aspects of streamline geometry

Curvilinear coordinates are the curvilinear abscissa s and the streamfunction ψ. An elementary displacement $\mathrm{d}\boldsymbol{M}$ is defined either by Cartesian coordinates $(\mathrm{d}x_1, \mathrm{d}x_2)$ in the fixed frame of reference or by $(\mathrm{d}s, \mathrm{d}\psi)$ in the Serret–Frenet frame, which is rotated at an angle, α say, from the fixed frame. Accordingly,

$$\mathrm{d}s = \cos(\alpha)\mathrm{d}x_1 + \sin(\alpha)\mathrm{d}x_2, \tag{A 1}$$

$$\mathrm{d}\psi = -U\sin(\alpha)\mathrm{d}x_1 + U\cos(\alpha)\mathrm{d}x_2, \tag{A 2}$$

from the expression of velocity in terms of the streamfunction: $U_i = \epsilon_{ij3}\partial\psi/\partial x_j$. The velocity modulus is of course $U = (U_1^2 + U_2^2)^{1/2}$. The above differential relationships (A 1) and (A 2) also yield $(\mathrm{d}s)^2 = (\mathrm{d}x_1)^2 + (\mathrm{d}x_2)^2$, and $\mathrm{d}s = U\mathrm{d}t$ at constant ψ. The angle α itself comes from

$$\mathrm{d}\alpha = \frac{\mathrm{d}s}{\mathscr{R}} + \beta\mathrm{d}\psi. \tag{A 3}$$

$\mathscr{R}$ is the local curvature radius and the coefficient β remains to be computed (see further derivation). The radius $\mathscr{R}$ is also defined by (see e.g. Sipp & Jacquin 2000)

$$\frac{U^3}{\mathscr{R}} = \frac{\partial\psi}{\partial x_i}U_j\frac{\partial U_i}{\partial x_j} \quad \text{or} \quad \psi_{,i}U_jU_{i,j}. \tag{A 4}$$

The intrinsic shear rate is

$$\mathscr{S}_h = \frac{U}{\mathscr{R}} - W/2 \tag{A 5}$$

with $W = U_{2,1} - U_{1,2}$.

From equations (A 2) and (A 4), one finds

$$\mathscr{S}_h = \tfrac{1}{2}\cos(2\alpha)(U_{2,1} + U_{1,2}) - \tfrac{1}{2}\sin(2\alpha)(U_{1,1} - U_{2,2}) \tag{A 6}$$

which means that $\mathscr{S}_h$ is the extra-diagonal term of the symmetrized gradient matrix in the Serret–Frenet axes. Let us define the angle α' as that of the principal axes of this symmetrized matrix with respect to the fixed frame. Equation (A 6) can then be rewritten as

$$\mathscr{S}_h = S\sin 2(\alpha - \alpha'), \tag{A 7}$$

in which S is the local strain rate. The symmetrized gradient matrix eigenvalues are $\pm S$ explicitly in the frame of its principal axes, which is also the reference frame

generated by its eigenvectors. This important result shows that $\mathscr{S}_h$ is bounded, at least with the crude relation $|\mathscr{S}_h| \leqslant S$.

It is also possible to express all the components of the gradient matrix $U_{i,j}$ using the curvilinear coordinates and equations (A 1), (A 2) and (A 3). Finding the divergence and the rotation is particularly interesting. The divergence is found to be

$$U_{1,1} + U_{2,2} = \frac{\partial U}{\partial s} + U^2 \frac{\partial \alpha}{\partial \psi} = 0 \tag{A 8}$$

from which the coefficient β in (A 3) is readily identified as $\beta = -(\partial U/\partial s)/U^2$. Similarly, the vorticity is

$$W = \frac{U}{\mathscr{R}} - \frac{1}{2}\frac{\partial (U^2)}{\partial \psi} \tag{A 9}$$

and finally the intrinsic shear rate given by (A 5) is

$$\mathscr{S}_h = \frac{1}{2}\frac{U}{\mathscr{R}} + \frac{1}{4}\frac{\partial (U^2)}{\partial \psi}. \tag{A 10}$$

The local strain rate S may then be rewritten as

$$S^2 = \mathscr{S}_h^2 + \left(\frac{\partial U}{\partial s}\right)^2. \tag{A 11}$$

Integrals over closed trajectories are also of some interest, using the property

$$\iint f(x_1, x_2)\, \mathrm{d}x_1 \mathrm{d}x_2 = \int_{\psi_0}^{\psi_1} \left(\int_0^{\mathscr{L}(\psi)} f(s, \psi) \frac{\mathrm{d}s}{U} \right) \mathrm{d}\psi$$

for surface integrals over the area delineated by a given trajectory $\psi = \psi_1$ of length $\mathscr{L}(\psi_1)$. For instance, using Stokes' theorem for expressing Γ,

$$\int_0^{\mathscr{L}(\psi)} \frac{1}{U} W(\psi)\, \mathrm{d}s = W(\psi) \int_0^{T(\psi)} \mathrm{d}t = W(\psi) T(\psi), \tag{A 12}$$

in which $T(\psi)$ is the period for evolving along the closed trajectory. The extremum of the absolute circulation is found from equation (A 12) to be

$$\frac{\mathrm{d}\Gamma_a}{\mathrm{d}\psi} = [W(\psi) + 2\Omega] T(\psi) \tag{A 13}$$

showing the coincidence of $\mathrm{d}\Gamma_a/\mathrm{d}\psi = 0$ and $W + 2\Omega = 0$.

By using the Stokes theorem for expressing $T(\psi)$ and (A 9)–(A 10), one finds

$$\frac{\mathrm{d}T}{\mathrm{d}\psi} = \int_0^T \frac{1}{U^2} \left(W + \frac{\partial U^2}{\partial \psi} \right) \mathrm{d}t = \int_0^T \frac{2\mathscr{S}_h}{U^2}\, \mathrm{d}t. \tag{A 14}$$

Appendix B. Additional results for the eikonal and vorticity equations

B.1. *Evolution of the wavevector*

We first show that the wavevector $\boldsymbol{k}$ solution of the eikonal equation cannot grow faster than algebraically (outside the hyperbolic stagnation point where exponential growth is possible). For this, we compute the evolution of $\boldsymbol{k} \cdot \boldsymbol{U}$ and $\boldsymbol{k} \cdot \nabla \psi$ along the trajectories (streamlines in the present case) of the basic flow with steady (Eulerian) velocity field $\boldsymbol{U}(\boldsymbol{x})$. This will be sufficient since $\boldsymbol{U}$ and $\nabla \psi$ are orthogonal, and thus

may be used to form an orthogonal basis (the Serret–Frenet frame, see Appendix A), after normalization by $|\boldsymbol{U}|$. Thus, the wavevector may be written as

$$\boldsymbol{k} = \frac{\boldsymbol{k}\cdot\boldsymbol{U}}{|\boldsymbol{U}|^2}\boldsymbol{U} + \frac{\boldsymbol{k}\cdot\nabla\psi}{|\boldsymbol{U}|^2}\nabla\psi + k_3\boldsymbol{n}, \tag{B 1}$$

where $\boldsymbol{n}$ is the unit vector normal to the plane of the flow.

We first obtain

$$\frac{\mathrm{d}}{\mathrm{d}t}(\boldsymbol{k}\cdot\boldsymbol{U}) = \frac{\mathrm{d}\boldsymbol{k}}{\mathrm{d}t}\cdot\boldsymbol{U} + \frac{\mathrm{d}\boldsymbol{U}}{\mathrm{d}t}\cdot\boldsymbol{k} = -(\boldsymbol{L}^T\boldsymbol{k})\cdot\boldsymbol{U} + (\boldsymbol{L}\boldsymbol{U})\cdot\boldsymbol{k} = 0, \tag{B 2}$$

where $\mathrm{d}/\mathrm{d}t$ is the Lagrangian derivative – also denoted with an overdot – and $\boldsymbol{L} = \nabla\boldsymbol{U}$ with components λ_{ij}. This gives $\boldsymbol{k}\cdot\boldsymbol{U} = c(\psi)$ (constant along the basic streamline, assumed positive), so that from (B 1)

$$\boldsymbol{k} = \frac{c(\psi)}{|\boldsymbol{U}|^2}\boldsymbol{U} + \frac{\boldsymbol{k}\cdot\nabla\psi}{|\boldsymbol{U}|^2}\nabla\psi. \tag{B 3}$$

Now, by taking into account that $\mathrm{d}\nabla\psi/\mathrm{d}t = -\boldsymbol{L}^T\nabla\psi$, it is easy to show that

$$\frac{\mathrm{d}}{\mathrm{d}t}(\boldsymbol{k}\cdot\nabla\psi) = -2(\boldsymbol{S}\nabla\psi)\cdot\boldsymbol{k}, \tag{B 4}$$

where $\boldsymbol{S} = \frac{1}{2}(\boldsymbol{L} + \boldsymbol{L}^T)$ is the symmetric velocity gradient tensor. Introducing the intrinsic shear $\mathscr{S}_h$ (see Appendix A) satisfying (Sipp & Jacquin 2000)

$$\mathscr{S}_h = \frac{1}{|\boldsymbol{U}|^2}(\boldsymbol{S}\nabla\psi)\cdot\boldsymbol{U}, \tag{B 5}$$

and taking into account the following relations:

$$\frac{\mathrm{d}}{\mathrm{d}t}|\boldsymbol{U}|^2 = \frac{\mathrm{d}}{\mathrm{d}t}|\nabla\psi|^2 = 2(\boldsymbol{S}\boldsymbol{U})\cdot\boldsymbol{U} = -2(\boldsymbol{S}\nabla\psi)\cdot\nabla\psi, \tag{B 6}$$

equation (B 4) may be written as, using (B 3):

$$\frac{\mathrm{d}}{\mathrm{d}t}\left(\frac{\boldsymbol{k}\cdot\nabla\psi}{|\boldsymbol{U}|^2}\right) = -2c(\psi)\frac{\mathscr{S}_h}{|\boldsymbol{U}|^2}. \tag{B 7}$$

We can then show that the left-hand side of (B 7) may be bounded along any streamline. Indeed, $-S_m(\psi) \leqslant \mathscr{S}_h \leqslant S_m(\psi)$, where $S_m(\psi)$ is the maximum eigenvalue of $\boldsymbol{S}$ along any streamline ψ (see Appendix A). Furthermore, we assume that $|\boldsymbol{U}|^2$ does not vanish along the streamline (stagnation points and separatrix are excluded from the analysis), and is finite, whereby $|\mathscr{S}_h|/|\boldsymbol{U}|^2$ may be bounded along each streamline by an appropriate positive constant $c'(\psi)$, such that $-c'(\psi) \leqslant \mathscr{S}_h/|\boldsymbol{U}|^2 \leqslant c'(\psi)$. As a consequence, integrating equation (B 7) gives

$$\frac{|\boldsymbol{k}\cdot\nabla\psi|}{|\boldsymbol{U}|^2} \leqslant 2c(\psi)c'(\psi)t + c_0, \tag{B 8}$$

using an initial constant c_0. Since $|\boldsymbol{U}|^2$ is assumed to be finite, $|\boldsymbol{k}\cdot\nabla\psi|$ cannot grow faster than algebraically along a regular streamline ψ.

Integrating (B 7) along a closed trajectory from instant $t = 0$ to T and using equation (A 14), one obtains

$$\left(\boldsymbol{k}\cdot\frac{\nabla\psi}{U}\right)_{t=T} - \left(\boldsymbol{k}\cdot\frac{\nabla\psi}{U}\right)_{t=0} = -\left(\boldsymbol{k}\cdot\frac{\boldsymbol{U}}{U}\right)_{t=0}\int_0^T \frac{2\mathscr{S}_h}{U^2}\,\mathrm{d}t = -\left(\boldsymbol{k}\cdot\frac{\boldsymbol{U}}{U}\right)_{t=0}\frac{\mathrm{d}T}{\mathrm{d}\psi}. \tag{B 9}$$

Therefore one sees that, for $\boldsymbol{k}$ to be periodic, one needs either $-(\boldsymbol{k}\cdot\boldsymbol{U}/U)_{t=0}=0$ (whence our choice of initial conditions), or $\mathrm{d}T/\mathrm{d}\psi=0$. The latter condition is exact for an extensional flow, and holds on stagnation points of elliptic or hyperbolic kind in general two-dimensional steady flows.

B.2. *Streamlines at zero absolute vorticity: $W(\psi)+2\Omega=0$*

We now proceed to show that any streamline ψ at zero absolute vorticity, i.e. such that $W(\psi)+2\Omega=0$, is exponentially stable to short-wavelength instabilities. For this, following Lifschitz (1994), we introduce the vorticity amplitude vector defined by

$$\boldsymbol{b}=\boldsymbol{k}\times\boldsymbol{a}\,,\qquad \boldsymbol{a}=-\frac{\boldsymbol{k}\times\boldsymbol{b}}{|\boldsymbol{k}|^2}, \tag{B 10}$$

with $\boldsymbol{b}\cdot\boldsymbol{k}=0$. Since $\boldsymbol{a}\cdot\boldsymbol{k}=0$ as well, it is easy to see that $|\boldsymbol{b}|=|\boldsymbol{k}|\,|\boldsymbol{a}|$, so that if $|\boldsymbol{k}|$ is bounded in time, the behaviours of $|\boldsymbol{b}|$ and $|\boldsymbol{a}|$ are similar. In a rotating frame, the vorticity amplitude is governed by

$$\frac{\mathrm{d}\boldsymbol{b}}{\mathrm{d}t}=\boldsymbol{L}\boldsymbol{b}-\boldsymbol{k}\cdot(\boldsymbol{W}+2\boldsymbol{\Omega})\frac{\boldsymbol{k}\times\boldsymbol{b}}{|\boldsymbol{k}|^2}. \tag{B 11}$$

At zero absolute vorticity, equation (B 11) simply yields $\mathrm{d}\boldsymbol{b}/\mathrm{d}t=\boldsymbol{L}\boldsymbol{b}$. Since the basic flow is two-dimensional, it is sufficient to study the evolution of the planar projection of $\boldsymbol{b}$, or equivalently $\boldsymbol{b}\cdot\boldsymbol{U}$ and $\boldsymbol{b}\cdot\nabla\psi$ as previously for the wavevector. Using similar arguments, it may be shown that

$$\frac{\mathrm{d}}{\mathrm{d}t}(\boldsymbol{b}\cdot\nabla\psi)=0, \tag{B 12}$$

and

$$\frac{\mathrm{d}}{\mathrm{d}t}(\boldsymbol{b}\cdot\boldsymbol{U})=2(\boldsymbol{S}\nabla\psi)\cdot\boldsymbol{b}, \tag{B 13}$$

and that $\boldsymbol{b}\cdot\nabla\psi$ is constant along a regular streamline ψ, whereas $|\boldsymbol{b}\cdot\boldsymbol{U}|$ cannot grow faster than algebraically.

For a closed streamline, the results (B 4), (B 7), (B 12) and (B 13) can be directly inferred from the shape of matrix $\boldsymbol{F}(\boldsymbol{X},0,T)$ (equation (3.16)) which can be expressed as

$$\begin{pmatrix}1&\gamma&0\\0&1&0\\0&0&1\end{pmatrix}$$

in the Serret–Frenet frame, where $\alpha=\mathrm{d}T/\mathrm{d}\psi$ (except in a neighbourhood of the hyperbolic stagnation points). The result from the eikonal equation comes from $\boldsymbol{k}=(\boldsymbol{F}^{-1})^T\boldsymbol{K}$ (in equation (3.16)), with

$$(\boldsymbol{F}^{-1})^T=\begin{pmatrix}1&0&0\\-\gamma&1&0\\0&0&1\end{pmatrix},$$

and another of the above-mentioned results arises from the vorticity equation written as the Cauchy solution

$$\boldsymbol{\omega}(\boldsymbol{x},t)=\boldsymbol{F}(\boldsymbol{X},0,T)\boldsymbol{\omega}(\boldsymbol{X},0)$$

again with $\boldsymbol{\omega}=\nabla\times\boldsymbol{u}$ at zero absolute vorticity.

We conclude that both $|\boldsymbol{b}|$ and $|\boldsymbol{a}|$ cannot grow faster than algebraically along any streamline at zero absolute vorticity (corresponding to an irrotational trajectory in

the fixed frame of reference). This extends the well-known result for the stabilization of the elliptical instability at zero absolute vorticity (Cambon *et al.* 1994; Leblanc 1997).

Finally, it is worth noting that this also shows that any steady planar irrotational flow in a non-rotating frame ($W = 0$ and $\Omega = 0$) is at most unstable to algebraically growing disturbances; exponential growth is only possible on the hyperbolic stagnation point. For Stuart vortices, this corresponds to the case $\rho = 1$. When $\Omega \neq 0$, this conclusion is no longer valid.

REFERENCES

Batchelor, G. K. & Proudman, I. 1954 The effect of rapid distortion on a fluid in turbulent motion. *Q. J. Mech. Appl. Maths* **7**, 83–103.

Bayly, B. J. 1986 Three-dimensional instability of elliptical flow. *Phys. Rev. Lett.* **57**, 2160–2163.

Bayly, B. J. 1988 Three-dimensional centrifugal-type instabilities in inviscid two-dimensional flows. *Phys. Fluids* **31**, 56–64.

Bayly, B. J., Holm, D. D. & Lifschitz, A. 1996 Three-dimensional stability of elliptical vortex columns in external strain flows. *Phil. Trans. R. Soc. Lond.* A **354**, 895–926.

Bidokhti, A. A. & Tritton, D. J. 1992 The structure of a turbulent free shear layer in a rotating fluid. *J. Fluid Mech.* **241**, 469–502.

Bradshaw, P. 1969 The analogy betweeen streamline curvature and buoyancy in turbulent shear flow. *J. Fluid Mech.* **36**, 177–191.

Cambon, C. 1982 Étude spectrale d'un champ turbulent incompressible soumis à des effets couplés de déformation et de rotation imposés extérieurement. PhD thesis, Université Lyon I, France.

Cambon, C. 2000 Stability of vortex structures in a rotating frame. In *Report on the Turbulence Programme*, *Scientific Programmes*. Isaac Newton Institute for Mathematical Science, Cambridge, UK.

Cambon, C., Benoît, J.-P., Shao, L. & Jacquin, L. 1994 Stability analysis and large eddy simulation of rotating turbulence with organized eddies. *J. Fluid Mech.* **278**, 175–200.

Cambon, C. & Scott, J. F. 1999 Linear and nonlinear models of anisotropic turbulence. *Ann. Rev. Fluid Mech.* **31**, 1–53.

Craik, A. D. D. 1989 The stability of unbounded two- and three-dimensional flows subject to body forces: some exact solutions. *J. Fluid Mech.* **198**, 275–292.

Craik, A. D. D. & Criminale, W. O. 1986 Evolution of wavelike disturbances in shear flows: a class of exact solutions of the Navier-Stokes equations. *Proc. R. Soc. Lond.* A **406**, 13–26.

Craya, A. 1958 Contribution à l'analyse de la turbulence associée à des vitesses moyennes. PST 345. Ministère de l'Air, France.

Drazin, P. G. & Reid, W. H. 1981 *Hydrodynamic Stability*. Cambridge University Press.

Hopfinger, E. J. & van Heijst, G. J. F. 1993 Vortices in rotating fluids. *Ann. Rev. Fluid Mech.* **25**, 241–289.

Johnson, J. A. 1963 The stability of shearing motion in a rotating fluid. *J. Fluid Mech.* **17**, 337–352.

Kelvin, Lord 1887 On the stability of steady and of periodic fluid motion. *Phil. Mag.* **27**, 188–196.

Kerr, O. S. & Dold, J. W. 1994 Periodic steady vortices in a stagnation-point flow. *J. Fluid Mech.* **276**, 307–325.

Kloosterziel, R. C. & van Heijst, G. J. F. 1991 An experimental study of unstable barotropic vortices in a rotating fluid. *J. Fluid Mech.* **223**, 1–24.

Lagnado, R. R. & Leal, L. G. 1990 Visualization of three-dimensional flow in a four-roll mill. *Exps. Fluids* **9**, 25–32.

Lagnado, R. R., Phan-Thien, N. & Leal, L. G. 1984 The stability of two-dimensional linear flows. *Phys. Fluids* **27**, 1094–1101.

Le Dizès, S. 2000 Three-dimensional instability of a multipolar vortex in a rotating flow. *Phys. Fluids* **12**, 2762–2774.

Le Duc, A. & Leblanc, S. 1999 A note on Rayleigh stability criterion for compressible flows. *Phys. Fluids* **11**, 3563–3566.

Leblanc, S. 1997 Stability of stagnation points in rotating flows. *Phys. Fluids* **9**, 3566–3569.

LEBLANC, S. 2000 Destabilization of a vortex by acoustic waves. *J. Fluid Mech.* **414**, 315–337.

LEBLANC, S. & CAMBON, C. 1997 On the three-dimensional instabilities of plane flows subjected to Coriolis force. *Phys. Fluids* **9**, 1307–1316.

LEBLANC, S. & CAMBON, C. 1998 Effects of the Coriolis force on the stability of Stuart vortices. *J. Fluid Mech.* **356**, 353–379.

LEBLANC, S. & GODEFERD, F. 1999 An illustration of the link between ribs and hyperbolic instability. *Phys. Fluids* **11**, 497–499.

LEBOVITZ, N. R. & LIFSCHITZ, A. 1996 Short-wavelength instabilities of Riemann ellipsoids. *Phil. Trans. R. Soc. Lond.* A **354**, 927–950.

LEWEKE, T. & WILLIAMSON, C. H. K. 1998 Cooperative elliptic instability of a vortex pair. *J. Fluid Mech.* **360**, 85–119.

LIFSCHITZ, A. 1991 Short wavelength instabilities of incompressible three-dimensional flows and generation of vorticity. *Phys. Lett.* A **157**, 481–487.

LIFSCHITZ, A. 1994 On the stability of certain motions of an ideal incompressible fluid. *Adv. Appl. Maths* **15**, 404–436.

LIFSCHITZ, A. & HAMEIRI, E. 1991 Local stability conditions in fluid dynamics. *Phys. Fluids* A **3**, 2644–2651.

LIGHTHILL, M. 1978 *Waves in Fluids*. Cambridge University Press.

LUNDGREN, T. & MANSOUR, N. 1996 Transition to turbulence in an elliptic vortex. *J. Fluid Mech.* **307**, 43–62.

MAJDA, A. 1984 *Compressible Fluid Flow and Systems of Conservation Laws in Several Space Variables*. Springer.

MOORE, D. W. & SAFFMAN, P. G. 1975 The instability of a straight vortex filament in a strain field. *Proc. R. Soc. Lond.* A **346**, 413–425.

PEDLEY, T. J. 1969 On the stability of viscous flow in a rapidly rotating pipe. *J. Fluid Mech.* **35**, 97–115.

PIERREHUMBERT, R. T. 1986 Universal short-wave instability of two-dimensional eddies in an inviscid fluid. *Phys. Rev. Lett.* **57**, 2157–2159.

PIERREHUMBERT, R. T. & WIDNALL, S. E. 1982 The two- and three-dimensional instabilities of a spatially periodic shear layer. *J. Fluid Mech.* **114**, 59–82.

POTYLITSIN, P. G. & PELTIER, W. R. 1998 Stratification effects on the stability of columnar vortices on the f-plane. *J. Fluid Mech.* **355**, 45–79.

POTYLITSIN, P. G. & PELTIER, W. R. 1999 Three-dimensional destabilization of Stuart vortices: the influence of rotation and ellipticity. *J. Fluid Mech.* **387**, 205–226.

SIPP, D. & JACQUIN, L. 1998 Elliptic instability in two-dimensional flattened Taylor–Green vortices. *Phys. Fluids* **10**, 839–849.

SIPP, D. & JACQUIN, L. 2000 Three-dimensional centrifugal-type instabilities of two-dimensional flows in rotating systems. *Phys. Fluids* **12**, 1740–1748.

SIPP, D., LAUGA, E. & JACQUIN, L. 1999 Vortices in rotating systems: Centrifugal, elliptic and hyperbolic type instabilities. *Phys. Fluids* **11**, 3716–3728.

SMYTH, W. & PELTIER, W. 1994 Three dimensionalization of barotropic vortices on the f-plane. *J. Fluid Mech.* **265**, 25–64.

STUART, J. T. 1967 On finite amplitude oscillations in laminar mixing layers. *J. Fluid Mech.* **29**, 417–440.

TOWNSEND, A. A. 1976 *The Structure of Turbulent Shear Flow*. Cambridge University Press.

TRITTON, D. 1988 *Physical Fluid Dynamics*, 2nd Edn. Clarendon.

TSAI, C. Y. & WIDNALL, S. E. 1976 The stability of short waves on a straight vortex filament in a weak externally imposed strain field. *J. Fluid Mech.* **73**, 721–733.

WALEFFE, F. 1990 On the three-dimensional instability of strained vortices. *Phys. Fluids* A **2**, 76–80.

YANASE, S., FLORES, C., MÉTAIS, O. & RILEY, J. 1993 Rotating free-shear flows. 1. Linear stability analysis. *Phys. Fluids* A **5**, 2725–2737.